

A Tensor-Structured Approach to Dynamic Channel Prediction for Massive MIMO Systems with Temporal Non-Stationarity

Hongwei Hou, *Graduate Student Member, IEEE*, Yafei Wang, *Graduate Student Member, IEEE*,
Yiming Zhu, *Graduate Student Member, IEEE*, Xinping Yi, *Member, IEEE*,
Wenjin Wang, *Member, IEEE*, Dirk T. M. Slock, *Fellow, IEEE*, Shi Jin, *Fellow, IEEE*

Abstract—In moderate- to high-mobility scenarios, channel state information (CSI) varies rapidly and becomes temporally non-stationary, leading to significant performance degradation in the channel reciprocity-dependent massive multiple-input multiple-output (MIMO) transmission. To address this challenge, we propose a tensor-structured approach to dynamic channel prediction (TS-DCP) for massive MIMO systems with temporal non-stationarity, which exploits both dual-timescale and cross-domain structured correlations. Specifically, due to the inherent spatial consistency, non-stationary channels on long-timescales are treated as stationary on short-timescales, decoupling complicated correlations into more tractable dual-timescale correlations. To exploit such property, we frame the pilot symbols, capturing short-timescale correlations within frames by Doppler domain modeling and long-timescale correlations across frames by Markov/autoregressive processes. Building upon this, we develop the tensor-structured received signal model in the spatial-frequency-temporal domain, incorporating correlated angle-delay-Doppler domain channels and Vandermonde-structured factor matrices. Furthermore, we model the cross-domain correlations within each frame, arising from the clustered distribution of scatterers, using the tensor-structured upgradation of the Markov process and coupled Gaussian distribution. Following these probabilistic models, we formulate the TS-DCP as the variational free energy (VFE) minimization problem, designing trial belief structures through online approximation and the Bethe method. This yields the online TS-DCP algorithm derived from a dual-layer VFE optimization process, where both outer and inner layers leverage the multilinear structure of channels to reduce the computational complexity significantly. Numerical simulations demonstrate the significant superiority of the proposed algorithm over benchmarks in terms of channel prediction performance.

Index Terms—Massive MIMO, channel prediction, variational inference, tensor representation

I. INTRODUCTION

Hongwei Hou, Yafei Wang, Yiming Zhu, and Wenjin Wang are with the National Mobile Communications Research Laboratory, Southeast University, Nanjing 210096, China, and also with Purple Mountain Laboratories, Nanjing 211100, China (e-mail: hongweihou@seu.edu.cn; wangyf@seu.edu.cn; ymzhu@seu.edu.cn; wangwj@seu.edu.cn).

Xinping Yi and Shi Jin are with the National Mobile Communications Research Laboratory, Southeast University, Nanjing 210096, China (e-mail: xyi@seu.edu.cn; jinshi@seu.edu.cn).

Dirk T. M. Slock is with the Department of Communication Systems, EURECOM, 06410 Biot, France (e-mail: Dirk.Slock@eurecom.fr).

DRIVEN by the demand for higher data rates, massive multiple-input multiple-output (MIMO) and orthogonal frequency-division multiplexing (OFDM) techniques are expected to keep playing vital roles in future communication systems thanks to their significant capacity gain and enhanced spectral efficiency [1]–[5]. In massive MIMO-OFDM systems, precoding and detection rely on the sufficiently accurate channel state information (CSI), making CSI acquisition critical in achieving high performance [6]–[8].

In time division duplex (TDD) systems, the channel reciprocity enables the acquisition of CSI in the uplink for use in the downlink, thus reducing CSI acquisition overhead. However, large Doppler frequencies and temporal non-stationarity in moderate- to high-mobility scenarios lead to severe channel aging, causing significant performance degradation. This issue becomes more challenging as future communication systems evolve to the upper mid-band [9], [10], due to the linearity of the Doppler frequency to the carrier frequency. To address these challenges, channel prediction has emerged as a promising solution, capturing temporal correlations in historical CSI to predict future CSI, thereby combating channel aging.

A. Previous Works

Doppler domain modeling demonstrates significant superiority among temporal correlation models for channel prediction in stationary environments. Specifically, [11] and [12] investigate Doppler frequency estimation by spectrum estimation algorithms for narrowband and wideband MIMO systems, respectively. Leveraging the high angle and delay resolution of massive MIMO-OFDM systems, the angle-delay domain channel estimation is performed, followed by Doppler frequency extraction from effective angle-delay domain channel taps [13]–[15]. To mitigate the effect of channel estimation error on channel prediction, [16] and [17] investigate the joint channel estimation and prediction in the angle-delay-Doppler domain. When it comes to the non-stationary channels, the time-varying Doppler frequencies are fitted by polynomials [18], thereby channel prediction can be done through the polynomial Fourier transformation and the orthogonal matching pursuit algorithm. By treating Doppler frequencies as imperfection parameters, the Doppler variations over time are also captured by autoregressive (AR) processes in [19], [20], which facilitate the exploitation of channel sparsity.

Beyond the Doppler domain modeling, the AR model has also been extensively investigated, especially in non-stationary environments. Specifically, the channel models based on angle and delay domain sparse representation are presented in [21]–[23], where AR processes depict the temporal correlation of sparse domain channels. As such, sparse Bayesian learning (SBL) and expectation maximization algorithms are employed for channel tracking and AR parameter learning. Incorporating the AR process of angle domain channels, [24] presents the online group SBL algorithm, which exploits the joint sparsity of the angle domain across subcarriers and the structured sparsity within one symbol. To further explore the inter-subcarrier correlations, angle-delay domain sparse representations are developed in [25], where spatial-temporal AR processes capture the residual temporal correlations of neighboring elements. Without the knowledge of array configurations, [26], [27] adopt high-order AR processes to describe temporal correlations of spatial domain channels, enhancing the robustness of channel prediction algorithms in practical systems. Due to the continuous evolution of propagation environments, the angle variations over time are still captured by AR processes and tracked by the Kalman filter (KF) [28]. In [29], [30], the Markov processes are introduced for the angle and angle-delay domain channel support, capturing the dynamic sparsity. Inspired by AR processes, [31] employs the Taylor series for temporal correlations of angle-delay domain channels and develops a linear regression-based algorithm.

B. Motivations and Contributions

Channel prediction in moderate- to high-mobility scenarios is challenging due to intractable temporal correlations arising from dynamic propagation environments. However, the inherent spatial consistency of wireless channels enables a practical simplification: non-stationary channels on long-timescales can be approximated as stationary on short-timescales [32]–[34], thus decoupling the complicated temporal correlations into more tractable dual-timescale correlations. Moreover, the clustered distribution of scatterers results in cross-domain correlations with significant structured patterns in both channel sparsity and power [35], [36]. By leveraging high-order structured probabilistic models, such correlations can be captured to align more effectively with practical channel characteristics, further enhancing the channel prediction performance.

In this paper, we investigate the tensor-structured approach to dynamic channel prediction (TS-DCP) for massive MIMO systems with temporal non-stationarity. The main contributions of this paper are summarized as follows:

- To exploit dual-timescale correlations, we frame the pilot symbols for channel prediction, characterizing the short- and long-timescale correlations by intra- and inter-frame correlations. Specifically, we develop the tensor-structured received signal model in the spatial-frequency-temporal domain, incorporating angle-delay-Doppler domain channels and Vandermonde-structured factor matrices to capture intra-frame correlations through Doppler domain modeling. Furthermore, Markov and AR processes are employed to model the hidden support and

value tensors, capturing inter-frame dynamic correlations of the angle-delay-Doppler domain channel.

- To capture cross-domain correlations, we introduce the concept of action regions, defined as the set of neighbors to the element of interest in each domain under tensor representations. Leveraging this concept, we upgrade the Markov process and coupled Gaussian distribution (CGD) to the Markov random field (MRF) and tensor-structured CGD (TCGD), respectively. These upgrades enable accurate modeling of correlated sparsity and power patterns among elements within the action regions, which align more effectively with the inherent characteristics of practical channels.
- Building on the probabilistic models, we formulate the TS-DCP as the variational free energy (VFE) minimization problem and present the online VFE approximation to reduce process latency and storage overhead. By designing trial belief structures using the Bethe method, the VFE minimization is converted into a dual-layer optimization process, yielding the online TS-DCP algorithm. The proposed algorithm leverages the multilinear structure of channels, enabling substantial reductions in computational complexity for both outer and inner layers. Numerical simulations demonstrate the significant superiority of the proposed algorithm over benchmarks in terms of channel prediction performance.

Organization: The rest of this paper is organized as below. Section II reviews the tensor definitions and operations. In Section III, we develop the channel model and its structured factor matrices. Based on probabilistic models in Section IV, the TS-DCP problem is formulated and approximated under the VFE minimization framework. The online TS-DCP algorithm is developed in Section V, and computational complexity is also analyzed. The superiority of the proposed algorithm is demonstrated through numerical simulations in Section VI. Finally, Section VII concludes the paper.

Notations: Throughout this paper, the imaginary unit is represented by $j = \sqrt{-1}$. x , \mathbf{x} , \mathbf{X} , and \mathcal{X} denote scalars, column vectors, matrices, and tensors, respectively. The transpose, conjugate, and conjugate-transpose operations are represented by the superscripts $(\cdot)^T$, $(\cdot)^*$, and $(\cdot)^H$, respectively. The symbols \mathbb{C} denote the complex number fields. $[\cdot]_{i_1, \dots, i_D}$ is the (i_1, \dots, i_D) -th element of D -order tensor. $\mathbb{D}\{\cdot\}$ and $\mathbb{H}\{\cdot\}$ denote the Kullback-Leibler (KL) divergence and differential entropy, respectively. The outer and Hadamard products are represented by the operator \circ and \odot , respectively. $\mathbb{E}\{\cdot\}$ and $\mathbb{V}\{\cdot\}$ denote the expectation and variance operators, respectively. $\text{diag}\{\cdot\}$ and $\text{Re}\{\cdot\}$ denote the diagonal and real part operators, respectively. $\text{CN}(\mathcal{X}; \mathbf{U}, \mathcal{E})$ denotes the element-wise circularly symmetric complex Gaussian distribution with mean \mathbf{U} and variance \mathcal{E} , where \mathcal{X} , \mathbf{U} , and \mathcal{E} are tensors of the same size. It implies that random variables following this distribution are uncorrelated. $\mathcal{C}(x)$ denotes the constant tensor with all elements being x . $\delta(\cdot)$, $\exp(\cdot)$, and $\ln(\cdot)$ denote the element-wise Dirac Delta, exponential, and logarithmic functions, respectively.

II. TENSOR PRELIMINARIES

In this section, we review the tensor definitions and operations used in this paper, and the reader interested in tensors can refer to [37].

Given the D -order tensor $\mathcal{X} \in \mathbb{C}^{N_1 \times N_2 \times \dots \times N_D}$, the mode- d fibers are defined by fixing the d -th dimension and varying the indices of remaining dimensions. The mode- d matrixization $\mathbf{X}_d \in \mathbb{C}^{N_d \times N_1 \dots N_{d-1} N_{d+1} \dots N_D}$ takes the mode- d fibers of \mathcal{X} as its column vectors. Specifically, the mode- d matrixization maps the tensor index (n_1, n_2, \dots, n_D) to the matrix index (n_d, j) , where $j = 1 + \sum_{m \neq d} (n_m - 1) J_m$ and $J_m = \prod_{k \neq m} N_k$. The high-order cyclic shift operations on tensors require specifying the dimension of operations, given by $[\mathcal{X}^{(d,k)}]_{\dots, n_d, \dots} = [\mathcal{X}]_{\dots, \bar{n}_d, \dots}$, where $\bar{n}_d = (n_d + k) \bmod N_d$.

Given the tensors \mathcal{X}, \mathcal{Y} with the same size, the inner product is defined as

$$\langle \mathcal{X}, \mathcal{Y} \rangle = \sum_{n_1} \sum_{n_2} \dots \sum_{n_D} [\mathcal{X}]_{n_1, n_2, \dots, n_D} [\mathcal{Y}]_{n_1, n_2, \dots, n_D}^* \quad (1)$$

which is also the high-order extension of matrix inner product, and we define $\|\mathcal{X}\|_F = \sqrt{\langle \mathcal{X}, \mathcal{X} \rangle}$ as the high-order extension of Frobenius norm. Besides, we define ℓ_1 norm of \mathcal{X} , given by $\|\mathcal{X}\|_1 = \sum_{n_1} \sum_{n_2} \dots \sum_{n_D} |[\mathcal{X}]_{n_1, n_2, \dots, n_D}|$.

The mode- d tensor-matrix multiplication of tensor \mathcal{X} and matrix $\mathbf{U}_d \in \mathbb{C}^{K_d \times N_d}$ is denoted as $\mathcal{Y} = \mathcal{X} \times_d \mathbf{U}_d$, where the elements of tensor-matrix multiplication are expressed as

$$[\mathcal{Y}]_{n_1, \dots, n_{d-1}, k_d, n_{d+1}, \dots, n_D} = \sum_{n_d} [\mathcal{X}]_{n_1, \dots, n_D} [\mathbf{U}]_{k_d, n_d} \quad (2)$$

The tensor-matrix multiplication $\mathcal{Y} = \mathcal{X} \times_d \mathbf{U}_d$ is equivalent to $\mathbf{Y}_d = \mathbf{U}_d \mathbf{X}_d$, and satisfies the commutativity across dimensions, given by

$$\mathcal{X} \times_m \mathbf{U}_m \times_d \mathbf{U}_d = \mathcal{X} \times_d \mathbf{U}_d \times_m \mathbf{U}_m \quad (m \neq d). \quad (3)$$

Based on the definition of tensor-matrix multiplication, the Tucker decomposition of given tensor \mathcal{X} is expressed as

$$\mathcal{X} = \mathcal{Z} \times_1 \mathbf{U}_1 \times_2 \dots \times_D \mathbf{U}_D, \quad (4)$$

where $\mathcal{Z} \in \mathbb{C}^{K_1 \times K_2 \times \dots \times K_D}$ and \mathbf{U}_d denote the core tensor and factor matrix, respectively.

III. SYSTEM MODEL

A. System Configuration and Frame Structure

We consider the massive MIMO-OFDM system with a base station (BS) equipped with a uniform planar array (UPA) of $N_{\text{an}} = N_h \times N_v$ antennas and single-antenna mobile terminals (MTs), where N_h and N_v denote the number of antennas in the horizontal and vertical directions, respectively.

This system operates in TDD mode with the frame structure shown in Fig. 1 and assumes perfect calibration, where channels are acquired from uplink training and then used for signal detection and precoding. The pilot and payload are allocated to different OFDM symbols to prevent overlap, while MTs employ comb-type pilot patterns within the pilot OFDM symbols to mitigate pilot contamination. With this configuration, the pilots for each MT are uniformly spaced at intervals of ΔT in the time domain and Δf in the frequency

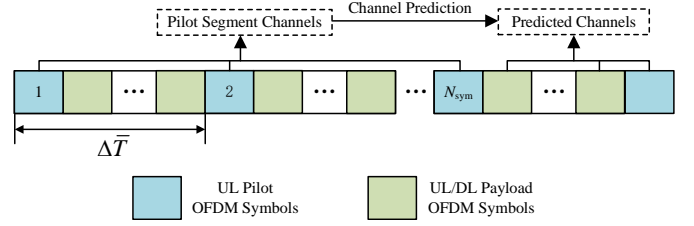


Fig. 1. Frame Structure of massive MIMO-OFDM systems in TDD mode.

domain, respectively. In this system, the BS collects the received symbols in the pilot segment and predicts channels of all symbols from the last current pilot symbol to the first future pilot symbol, thus combating channel aging.

B. Channel and Signal Models

Since wireless channels have inherent spatial consistency in practical systems, the physical parameters of each path remain unchanged within frames and vary smoothly across frames [32]–[34]. Therefore, the channel impulse response (CIR) at the (n_h, n_v) -th antenna and the n_F -th frame is expressed as¹

$$h_{n_F, n_h, n_v}(t, \tau) = \sum_{l=1}^{L_{n_F}} g_{n_F, l} e^{j2\pi t \nu_{n_F, l}} \delta(\tau - \tau_{n_F, n_h, n_v, l}), \quad (5)$$

where L_{n_F} denotes the number of paths, $\tau_{n_F, n_h, n_v, l} \triangleq \tau_{n_F, l} + (n_h - 1)\theta_{n_F, l} + (n_v - 1)\phi_{n_F, l}$ and $\tau_{n_F, l}$ denote the propagation delay of the l -th path from the MT to the (n_h, n_v) -th and reference antenna under the far-field assumption, respectively, $g_{n_F, l}$ and $\nu_{n_F, l}$ denote the path gain and Doppler frequency of the l -th path, respectively, $\theta_{n_F, l} \triangleq d \sin(\psi_{\text{el}, n_F, l}) \sin(\psi_{\text{az}, n_F, l}) / c$ and $\phi_{n_F, l} \triangleq d \cos(\psi_{\text{el}, n_F, l}) / c$ denote the horizontal and vertical directional cosine of the l -th path, respectively, $\psi_{\text{el}, n_F, l}$ and $\psi_{\text{az}, n_F, l}$ denote the elevation and azimuth angle of the l -th path, respectively.

Due to the sufficiently small OFDM symbol duration in practical systems, the CIRs are assumed to be constant within one OFDM symbol [16], [17]. Therefore, by taking the Fourier transform of CIRs and stacking the result in all antennas and pilot resource elements in the n_F -th frame, the spatial-frequency-temporal domain channel tensor at pilot segments is given as

$$\mathcal{H}_{n_F} = \sum_{l=1}^{L_{n_F}} g_{n_F, l} \mathbf{a}_h(\theta_{n_F, l}) \circ \mathbf{a}_v(\phi_{n_F, l}) \circ \mathbf{b}(\tau_{n_F, l}) \circ \mathbf{c}(\nu_{n_F, l}), \quad (6)$$

where $\mathbf{a}_h(\theta)$, $\mathbf{a}_v(\phi)$, $\mathbf{b}(\tau)$ and $\mathbf{c}(\nu)$ denote the horizontal angle, vertical angle, delay and Doppler domain steering vectors, defined by $[\mathbf{a}_h(\theta)]_{n_h} \triangleq \exp(-j2\pi(n_h - 1)\theta)$, $[\mathbf{a}_v(\phi)]_{n_v} \triangleq \exp(-j2\pi(n_v - 1)\phi)$, $[\mathbf{b}(\tau)]_{n_{\text{sc}}} \triangleq \exp(-j2\pi(n_{\text{sc}} - 1)\Delta f \tau)$ and $[\mathbf{c}(\nu)]_{n_{\text{sym}}} \triangleq \exp(j2\pi(n_{\text{sym}} - 1)\Delta T \nu)$, respectively.

¹Since there is no pilot contamination between MTs, we focus on the typical MT in the cell and ignore the MT index for simplicity of expressions.

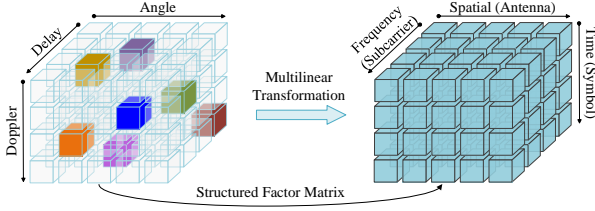


Fig. 2. The diagrams of the spatial-frequency-temporal domain and angle-delay-Doppler domain channel tensors. In this case, only one of the angle domains and one of the antenna domains are shown.

After the cyclic prefix removal and OFDM demodulation, the received signal tensor at pilot segments in the spatial-frequency-temporal domain is expressed as

$$\mathcal{Y}_{n_F} = \mathcal{X} \odot \mathcal{H}_{n_F} + \mathcal{Z}_{n_F}, \quad (7)$$

where $\mathcal{X} \in \mathbb{C}^{N_h \times N_v \times N_{\text{sym}} \times N_{\text{sc}}}$, $\mathcal{H}_{n_F} \in \mathbb{C}^{N_h \times N_v \times N_{\text{sym}} \times N_{\text{sc}}}$ and $\mathcal{Z}_{n_F} \in \mathbb{C}^{N_h \times N_v \times N_{\text{sym}} \times N_{\text{sc}}}$ denote the pilot tensor, the spatial-frequency-temporal domain channel and the additive white Gaussian noise at pilot segments, respectively. Since the pilot symbols in the uplink training phase are known at BS, we assume that $\mathcal{X} \triangleq \mathcal{C}(1)$ without loss of generality.

C. Vandermonde-Structured Factor Matrices

Since scatterers in wireless channels are limited, the spatial-frequency-temporal domain channel tensor exhibits low-rank characterizations, which can be exploited by the tensor decomposition (TD) framework. However, the conventional TD algorithms involve the uniqueness condition [38], which is typically not fulfilled in practical propagation environments.

To address such issue, a promising approach is exploring the structured information inherent in factor matrices [39]–[41]. Based on the channel model in (6), the factor matrices have Vandermonde structures, defined as

$$\tilde{\mathbf{A}}_h(\tilde{\boldsymbol{\theta}}_{n_F}) = [\mathbf{a}_h(\tilde{\theta}_{1,n_F}), \mathbf{a}_h(\tilde{\theta}_{2,n_F}), \dots, \mathbf{a}_h(\tilde{\theta}_{K_h,n_F})], \quad (8a)$$

$$\tilde{\mathbf{A}}_v(\tilde{\boldsymbol{\phi}}_{n_F}) = [\mathbf{a}_v(\tilde{\phi}_{1,n_F}), \mathbf{a}_v(\tilde{\phi}_{2,n_F}), \dots, \mathbf{a}_v(\tilde{\phi}_{K_v,n_F})], \quad (8b)$$

$$\tilde{\mathbf{B}}(\tilde{\boldsymbol{\tau}}_{n_F}) = [\mathbf{b}(\tilde{\tau}_{1,n_F}), \mathbf{b}(\tilde{\tau}_{2,n_F}), \dots, \mathbf{b}(\tilde{\tau}_{K_{\text{de}},n_F})], \quad (8c)$$

$$\tilde{\mathbf{C}}(\tilde{\boldsymbol{\nu}}_{n_F}) = [\mathbf{c}(\tilde{\nu}_{1,n_F}), \mathbf{c}(\tilde{\nu}_{2,n_F}), \dots, \mathbf{c}(\tilde{\nu}_{K_{\text{do}},n_F})], \quad (8d)$$

where $\mathcal{K}_x \triangleq \{1, 2, \dots, K_x\}$, $\mathbf{x} \in \{h, v, de, do\}$ denotes the index set of varying generators, K_h , K_v , K_{de} and K_{do} control the trade-off between computational complexity and decomposition performance, $\tilde{\chi}_{k,n_F}$, $\chi \in \{\theta, \phi, \tau, \nu\}$ denote the varying generators in horizontal angle, vertical angle, delay and Doppler domains in the n_F -th frame, respectively.

Based on structured factor matrices, the spatial-frequency-time domain channel tensor can be decomposed as

$$\mathcal{H}_{n_F} = \mathcal{G}_{n_F} \times_1 \tilde{\mathbf{A}}_h(\tilde{\boldsymbol{\theta}}_{n_F}) \times_2 \tilde{\mathbf{A}}_v(\tilde{\boldsymbol{\phi}}_{n_F}) \times_3 \tilde{\mathbf{B}}(\tilde{\boldsymbol{\tau}}_{n_F}) \times_4 \tilde{\mathbf{C}}(\tilde{\boldsymbol{\nu}}_{n_F}), \quad (9)$$

where $\mathcal{G}_{n_F} \in \mathbb{C}^{K_h \times K_v \times K_{\text{de}} \times K_{\text{do}}}$ denotes the core tensor in the angle-delay-Doppler domain. The spatial-frequency-temporal domain and angle-delay-Doppler domain channel tensors are illustrated in Fig. 2, with one angle domain and one antenna domain depicted for clarity.

Remark 1. Due to the inherent spatial consistency of channels, we assume that the physical parameters of each path remain unchanged for sufficiently short durations. This assumption allows temporal correlations within the frames to be captured by Doppler domain modeling in (9), facilitating subsequent channel prediction.

IV. PROBLEM FORMULATION

A. Probabilistic Model

Besides the uniqueness conditions, the multilinear rank required by conventional TD algorithms is typically unavailable or costly to acquire. Such challenges can be addressed by the Bayesian framework, which enables automatic rank determination, thus eliminating the need for multilinear rank acquisition [42]–[44]. Therefore, we develop probabilistic models to capture the inherent structured sparsity in the wireless channels and formulate the Bayesian TS-DCP problem.

1) *Observation and Multilinear Transformation:* Based on the channel and signal models, the probability density functions (PDFs) for the observation model and multilinear transformation model are expressed as

$$P(\mathcal{Y}_{(N_F)} | \mathcal{H}_{(N_F)}) = \prod_{n_F=1}^{N_F} P(\mathcal{Y}_{n_F} | \mathcal{H}_{n_F}), \quad (10a)$$

$$P(\mathcal{H}_{(N_F)} | \mathcal{G}_{(N_F)}, \mathcal{P}_{\text{ML},(N_F)}) = \prod_{n_F=1}^{N_F} P(\mathcal{H}_{n_F} | \mathcal{G}_{n_F}, \mathcal{P}_{\text{ML},n_F}), \quad (10b)$$

respectively, where $\mathcal{Y}_{(N_F)} \triangleq \{\mathcal{Y}_{n_F}\}_{n_F=1}^{N_F}$ denotes the sets of observations, $\mathcal{H}_{(N_F)} \triangleq \{\mathcal{H}_{n_F}\}_{n_F=1}^{N_F}$ and $\mathcal{G}_{(N_F)} \triangleq \{\mathcal{G}_{n_F}\}_{n_F=1}^{N_F}$ denote the sets of spatial-frequency-temporal domain channel and angle-delay-Doppler domain channel tensors, respectively, $\mathcal{P}_{\text{ML},(N_F)} \triangleq \cup_{n_F=1}^{N_F} \mathcal{P}_{\text{ML},n_F}$ denotes the sets of multilinear generators in all frames, $\mathcal{P}_{\text{ML},n_F} \triangleq \{\tilde{\boldsymbol{\theta}}_{n_F}, \tilde{\boldsymbol{\phi}}_{n_F}, \tilde{\boldsymbol{\tau}}_{n_F}, \tilde{\boldsymbol{\nu}}_{n_F}\}$ denotes the sets of multilinear generators in the n_F -th frame. The observation model and multilinear transformation model in the n_F -th frame are defined as

$$P(\mathcal{Y}_{n_F} | \mathcal{H}_{n_F}) \propto \text{CN}(\mathcal{Y}_{n_F}; \mathcal{H}_{n_F}, \mathcal{C}(\sigma_z^2)), \quad (11a)$$

$$P(\mathcal{H}_{n_F} | \mathcal{G}_{n_F}, \mathcal{P}_{\text{ML},(N_F)}) \propto \delta(\mathcal{H}_{n_F} - \mathcal{G}_{n_F} \times_1 \tilde{\mathbf{A}}_h(\tilde{\boldsymbol{\theta}}_{n_F}) \times_2 \tilde{\mathbf{A}}_v(\tilde{\boldsymbol{\phi}}_{n_F}) \times_3 \tilde{\mathbf{B}}(\tilde{\boldsymbol{\tau}}_{n_F}) \times_4 \tilde{\mathbf{C}}(\tilde{\boldsymbol{\nu}}_{n_F})), \quad (11b)$$

respectively.

Remark 2. The multilinear transformation in (11) exploits the separable dictionary structures of spatial-frequency-temporal domain channels, encompassing conventional linear transformations as a special case. This representation enables the proposed TS-DCP algorithm to achieve significant computational complexity reductions, as detailed in subsequent analysis.

2) *Dynamic and Clustered Correlations:* Beyond short-timescale correlation modeling based on the Doppler domain, capturing long-timescale and cross-domain structured correlations can facilitate more accurate channel prediction.

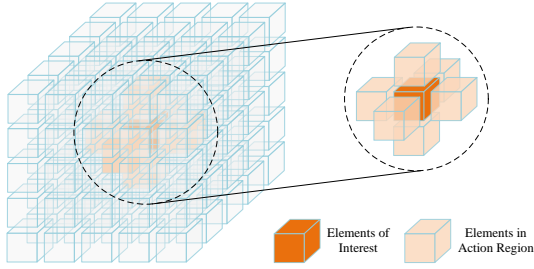


Fig. 3. The three-dimensional schematic of action regions. In this case, $\mathcal{N} \triangleq \{(1, 1), (1, -1), (2, 1), (2, -1), (3, 1), (3, -1)\}$.

Specifically, we model angle-delay-Doppler domain channel tensors by two hidden random processes, expressed as

$$P(\mathcal{G}_{(N_F)} | \mathcal{S}_{(N_F)}, \mathcal{Q}_{(N_F)}) = \prod_{n_F=1}^{N_F} \frac{\delta(\mathcal{G}_{n_F} - \mathcal{S}_{n_F} \odot \mathcal{Q}_{n_F})}{P(\mathcal{G}_{n_F} | \mathcal{S}_{n_F}, \mathcal{Q}_{n_F})}, \quad (12)$$

where $\mathcal{S}_{(N_F)} \triangleq \{\mathcal{S}_{n_F}\}_{n_F=1}^{N_F}$, and $\mathcal{Q}_{(N_F)} \triangleq \{\mathcal{Q}_{n_F}\}_{n_F=1}^{N_F}$, the binary-valued tensor \mathcal{S}_{n_F} and complex-valued tensor \mathcal{Q}_{n_F} describe the sparsity and power of the angle-delay-Doppler domain channel, respectively. Since angle-delay-Doppler domain channel tensor elements that are not visible in one frame may become visible in subsequent frames under temporally non-stationary environments, it is crucial to employ hidden value tensors for the modeling of all potential path gains [29].

Due to the smooth variation of the physical parameters of each path across frames, the hidden support tensor is modeled as a first-order Markov process, given by

$$P(\mathcal{S}_{(N_F)}; \mathcal{M}) = \prod_{n_F=1}^{N_F} P(\mathcal{S}_{n_F} | \mathcal{S}_{n_F-1}; \mathcal{M}), \quad (13)$$

where $\mathcal{S}_0 \triangleq \mathcal{C}(0)$, \mathcal{M} denotes the transition factor and controls the sparsity transition probability across frames. In this model, $P(\mathcal{S}_{n_F} | \mathcal{S}_{n_F-1}; \mathcal{M})$ denotes the transition probabilistic models of the hidden support tensor, given by

$$P(\mathcal{S}_{n_F} | \mathcal{S}_{n_F-1}; \mathcal{M}) = P_{\text{MRF}}(\mathcal{S}_{n_F}) P_{\text{TC}}(\mathcal{S}_{n_F} | \mathcal{S}_{n_F-1}; \mathcal{M}), \quad (14)$$

where $P_{\text{TC}}(\mathcal{S}_{n_F} | \mathcal{S}_{n_F-1}; \mathcal{M})$ denotes the long-timescale probabilistic model across frames, given by

$$P_{\text{TC}}(\mathcal{S}_{n_F} | \mathcal{S}_{n_F-1}; \mathcal{M}) \propto \exp(\langle \mathcal{M} \odot (2\mathcal{S}_{n_F-1} - 1), (2\mathcal{S}_{n_F} - 1) \rangle), \quad (15)$$

where the conversion from binary to bipolar support tensor is inspired by the Ising model [45]–[47] and $P_{\text{MRF}}(\mathcal{S}_{n_F})$ denotes the intra-frame cross-domain probabilistic model, given by

$$P_{\text{MRF}}(\mathcal{S}_{n_F}) \propto \prod_{(d,k) \in \mathcal{N}} \exp(C_{\text{HO}} \langle (2\mathcal{S}_{n_F} - 1), (2\mathcal{S}_{n_F}^{(d,k)} - 1) \rangle), \quad (16)$$

where \mathcal{N} denotes the action region of cross-domain correlations, the scalar-valued hyperparameter C_{HO} controls the cross-domain structured sparsity and the larger C_{HO} implying the more significant clustered sparsity pattern. A three-dimensional example of the action region is shown in Fig. 3,

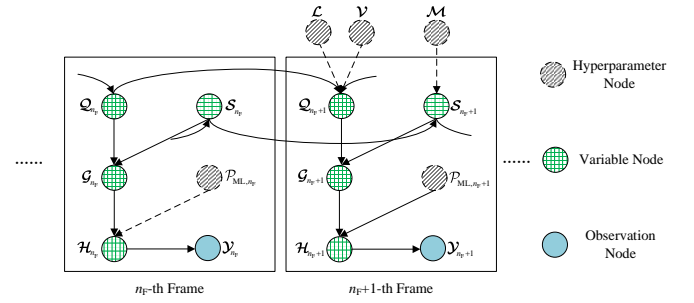


Fig. 4. Hierarchical Bayesian model for TS-DCP problem.

for $(d, k) \in \mathcal{N}$, it indicates that the correlation exists between elements separated by k grids along the d -th dimension.²

Similarly, the hidden value tensor is modeled based on the hidden value tensor of the previous frame, given by

$$\mathcal{Q}_{n_F} = (1 - \mathcal{L}) \odot \mathcal{Q}_{n_F-1} + \mathcal{L} \odot \mathcal{W}, \quad (17)$$

where \mathcal{L} denotes the transition factor and controls the long-timescale temporal correlations, $\mathcal{Q}_0 \triangleq \mathcal{C}(0)$, \mathcal{W} denotes the perturbation tensor following TCGD and controls the variations of hidden value tensor across frames, given by

$$P(\mathcal{W}) \propto \text{CN}(\mathcal{W}; 0, \mathcal{V}) \prod_{(d,k) \in \mathcal{N}} \text{CN}(\mathcal{W}; 0, C_{\text{HO}}^{-1} \mathcal{V}^{(d,k)}). \quad (18)$$

It implies that the power of each element in the perturbation tensor is controlled not only by its hyperparameter but also by the hyperparameters within \mathcal{N} .

Remark 3. We assume that the temporal variations of hyperparameters are negligible, allowing for the joint processing of multiple frames to enhance hyperparameter learning accuracy. It is typically satisfied in practical propagation environments by carefully selecting the number of frames used for learning.

B. TS-DCP Problem Formulation and Online Approximation

Building on the above probabilistic models, the hierarchical Bayesian model is depicted in Fig. 4, where the interaction between two frames is shown for simplicity. Therefore, the acquisition of angle-delay-Doppler domain channel tensors based on the minimum mean square error (MMSE) criterion is expressed as

$$\hat{\mathcal{G}}_{(N_F)} = \int \mathcal{G}_{(N_F)} P(\mathcal{G}_{(N_F)} | \mathcal{Y}_{(N_F)}, \mathcal{P}_{\text{ML},(N_F)}; \mathcal{P}_{\text{HP}}), \quad (19)$$

where $P(\mathcal{G}_{(N_F)} | \mathcal{Y}_{(N_F)}, \mathcal{P}_{\text{ML},(N_F)}; \mathcal{P}_{\text{HP}})$ denotes the marginal posterior PDF, $\mathcal{P}_{\text{HP}} \triangleq \{\mathcal{M}, \mathcal{L}, \mathcal{V}\}$ denotes the set of hyperparameters.

The marginal posterior PDF involves multiple integrals of the joint posterior PDF, resulting in prohibitive computational complexity for the MMSE estimator in massive MIMO systems. To address this, we apply the variational inference approach, approximating the posterior PDF using trial beliefs.

²Note that we assume the monotonicity of generators in the structured factor matrices without loss of generality, given by $\chi_{1,n_F} < \chi_{2,n_F} < \dots < \chi_{K_x,n_F}$, where $\chi \in \{\theta, \phi, \tau, \nu\}$ and $x \in \{h, v, de, do\}$.

Based on the KL-divergence minimization criterion, the posterior PDF approximation is expressed by

$$\hat{\mathbf{b}} = \arg \min_{\mathbf{b}} F_V, \quad (20)$$

where $\mathbf{b} \triangleq \mathbf{b}(\mathcal{H}_{(N_F)}, \mathcal{G}_{(N_F)}, \mathcal{S}_{(N_F)}, \mathcal{Q}_{(N_F)}, \mathcal{P}_{ML,(N_F)}; \mathcal{P}_{HP})$ denotes the trial belief, F_V denotes the joint VFE defined as the KL divergence between trial belief and joint PDF. The straightforward approach for VFE minimization involves storing all received signals and performing joint optimization of the trial belief across all frames. As the number of frames increases, this approach results in significant storage overhead, computational complexity, and processing latency.

Based on the properties of KL divergence, when trial beliefs can be factorized into per-frame trial beliefs without shared variables, the joint VFE can be decomposed into the sum of per-frame VFEs. However, due to hyperparameters shared across frames and variables common to successive frames in probabilistic models, the trial belief in the joint VFE minimization problem is generally unfactorizable.

To address this issue, we exploit the slow variation of hyperparameters and constrain the trial belief as the factorized form, given by

$$\mathbf{b}(\mathcal{H}_{(N_F)}, \mathcal{G}_{(N_F)}, \mathcal{S}_{(N_F)}, \mathcal{Q}_{(N_F)}, \mathcal{P}_{ML,(N_F)}; \mathcal{P}_{HP}) = \mathbf{b}(\mathcal{P}_{HP})\mathbf{b}(\mathcal{H}_{(N_F)}, \mathcal{G}_{(N_F)}, \mathcal{S}_{(N_F)}, \mathcal{Q}_{(N_F)}, \mathcal{P}_{ML,(N_F)}), \quad (21)$$

where the hyperparameter beliefs are constrained to uninformative Dirac-Delta functions, expressed by

$$\mathbf{b}(\mathcal{P}_{HP}) = \mathbf{b}(\mathcal{M})\mathbf{b}(\mathcal{L})\mathbf{b}(\mathcal{V}), \quad (22a)$$

$$\mathbf{b}(\mathcal{P}) = \delta(\mathcal{P} - \hat{\mathcal{P}}), \mathcal{P} \in \{\mathcal{M}, \mathcal{L}, \mathcal{V}\} \quad (22b)$$

where $\hat{\mathcal{P}}$ denotes the ground-truth hyperparameters. Furthermore, for the common variables across successive frames, we approximate the variables of the previous frame by the posterior mean [30], decoupling the trial beliefs as

$$\mathbf{b}(\mathcal{H}_{(N_F)}, \mathcal{G}_{(N_F)}, \mathcal{S}_{(N_F)}, \mathcal{Q}_{(N_F)}, \mathcal{P}_{ML,(N_F)}) \approx \prod_{n_F=1}^{N_F} \mathbf{b}(\mathcal{H}_{n_F}, \mathcal{G}_{n_F}, \mathcal{S}_{n_F}, \mathcal{Q}_{n_F}, \mathcal{P}_{ML,n_F}). \quad (23)$$

It implies that optimizing trial beliefs within each frame depends solely on past observations, which aligns with the VFE interpretation of the filtering mode discussed in [48].

Building on the design of trial beliefs, the joint VFE minimization is reformulated as a dual-layer optimization, with the outer layer focused on hyperparameter learning and the inner layer on per-frame VFE minimization. Therefore, the TS-DCP operates in an online manner, restricting the optimization of trial beliefs to a single frame, given by

$$\hat{\mathbf{b}}_{n_F} = \arg \min_{\mathbf{b}_{n_F}} \bar{F}_{V,n_F}, \quad (24)$$

where $\mathbf{b}_{n_F} \triangleq \mathbf{b}(\mathcal{H}_{n_F}, \mathcal{G}_{n_F}, \mathcal{S}_{n_F}, \mathcal{Q}_{n_F}, \mathcal{P}_{ML,n_F})$ denotes the per-frame trial belief, \bar{F}_{V,n_F} denotes the per-frame VFE given by (25) at the top of the next page, $\hat{\mathcal{P}}_{HP} \triangleq \{\mathcal{M}, \mathcal{L}, \mathcal{V}\}$ denotes the set of hyperparameters learned by the outer layer.

Beyond the design of trial belief structures for online approximation, inspired by hyperparameter belief structures,

we constrain the trial belief of the n_F -th frame to the factorized form with respect to its generators, given by

$$\mathbf{b}(\mathcal{H}_{n_F}, \mathcal{G}_{n_F}, \mathcal{S}_{n_F}, \mathcal{Q}_{n_F}, \mathcal{P}_{ML,n_F}) = \mathbf{b}(\mathcal{P}_{ML,n_F})\mathbf{b}(\mathcal{H}_{n_F}, \mathcal{G}_{n_F}, \mathcal{S}_{n_F}, \mathcal{Q}_{n_F}), \quad (26)$$

where the beliefs of the generators are constrained to uninformative Dirac-Delta functions, expressed by

$$\mathbf{b}(\mathcal{P}_{ML,n_F}) = \mathbf{b}(\tilde{\boldsymbol{\theta}}_{n_F})\mathbf{b}(\tilde{\boldsymbol{\phi}}_{n_F})\mathbf{b}(\tilde{\boldsymbol{\tau}}_{n_F})\mathbf{b}(\tilde{\boldsymbol{\nu}}_{n_F}), \quad (27a)$$

$$\mathbf{b}(\tilde{\boldsymbol{\chi}}_{n_F}) = \delta(\tilde{\boldsymbol{\chi}}_{n_F} - \hat{\boldsymbol{\chi}}_{n_F}), \boldsymbol{\chi} \in \{\boldsymbol{\theta}, \boldsymbol{\phi}, \boldsymbol{\tau}, \boldsymbol{\nu}\} \quad (27b)$$

where $\hat{\boldsymbol{\chi}}_{n_F}$ denotes the generators learned by the outer layer.

V. ONLINE TENSOR-STRUCTURED DYNAMIC CHANNEL PREDICITION ALGORITHM

A. Alternating VFE Minimization for Online TS-DCP

In prior efforts on Bayesian TD, the beliefs of different variables are typically assumed to be independent, neglecting the dependencies between auxiliary beliefs, which results in significant exactness loss. To address this issue, we represent the VFE minimization as alternating minimization of the multilinear observation (MO) and structured prior (SP) modules, shown in Fig. 5. This representation facilitates the incorporation of module-specific variable dependencies, thereby balancing accuracy and computational tractability.

1) *MO Module*: Since the MO model is a multilinear generalization of the linear observation model, we employ the Bethe method [49]–[51] based on joint PDF factorization and region partitioning, which characterizes global dependencies between beliefs with marginal consistency constraints (MCCs). Specifically, the trial belief is expressed as

$$\mathbf{b}_{MO} = \frac{\mathbf{b}_{Y,n_F} \mathbf{b}_{HG,n_F} \mathbf{b}_{G,n_F}}{\mathbf{f}_{H,n_F} \mathbf{f}_{G,n_F}^N} \quad (28)$$

where \mathbf{b}_{Y,n_F} , \mathbf{b}_{HG,n_F} , \mathbf{b}_{G,n_F} , \mathbf{f}_{H,n_F} , \mathbf{f}_{G,n_F} are introduced for (11a) and (11b), the prior PDF from the SP module, \mathcal{H}_{n_F} and \mathcal{G}_{n_F} , respectively, and $N \triangleq N_h N_v N_{sc} N_{sym}$.

Therefore, the VFE in the MO module is converted to the Bethe free energy (BFE), expressed as

$$\begin{aligned} F_{MO,n_F} = & D[\mathbf{b}_{Y,n_F} \parallel \mathbf{P}(\mathcal{Y}_{n_F} | \mathcal{H}_{n_F})] + D[\mathbf{b}_{G,n_F} \parallel \mathbf{P}(\mathcal{G}_{n_F})] + \\ & D[\mathbf{b}_{HG,n_F} \parallel \mathbf{P}(\mathcal{H}_{n_F} | \mathcal{G}_{n_F}, \hat{\mathcal{P}}_{ML,n_F})] + H[\mathbf{f}_{H,n_F}] + \\ & NH[\mathbf{f}_{G,n_F}], \end{aligned} \quad (29)$$

where $\mathbf{P}(\mathcal{G}_{n_F})$ denotes the prior PDF approximation of angle-delay-Doppler domain channel tensors from the SP module. Following this construction, the VFE minimization in this module is formulated as the BFE minimization with MCCs of factor and variable beliefs.

Since the MCCs for continuous random variables are still intractable, we relax them to sufficient statistics consistency constraints (SSCCs). Specifically, the first-order (FO) and second-order (SO) SSCCs are denoted as

$$E_{\mathbf{b}_{Y,n_F}} \{\mathcal{H}_{n_F}\} = E_{\mathbf{b}_{HG,n_F}} \{\mathcal{H}_{n_F}\} = E_{\mathbf{f}_{H,n_F}} \{\mathcal{H}_{n_F}\}, \quad (30a)$$

$$E_{\mathbf{b}_{HG,n_F}} \{\mathcal{G}_{n_F}\} = E_{\mathbf{b}_{G,n_F}} \{\mathcal{G}_{n_F}\} = E_{\mathbf{f}_{G,n_F}} \{\mathcal{G}_{n_F}\}, \quad (30b)$$

$$V_{\mathbf{b}_{Y,n_F}} \{\mathcal{H}_{n_F}\} = V_{\mathbf{b}_{HG,n_F}} \{\mathcal{H}_{n_F}\} = V_{\mathbf{f}_{H,n_F}} \{\mathcal{H}_{n_F}\}, \quad (30c)$$

$$\bar{F}_{V,n_F} \triangleq D[b(\mathcal{H}_{n_F}, \mathcal{G}_{n_F}, \mathcal{S}_{n_F}, \mathcal{Q}_{n_F}, \mathcal{P}_{ML,n_F}) \parallel P(\mathcal{H}_{n_F}, \mathcal{G}_{n_F}, \mathcal{S}_{n_F}, \mathcal{Q}_{n_F}, \mathcal{Y}_{n_F} \mid \mathcal{S}_{n_F-1}, \mathcal{Q}_{n_F-1}, \mathcal{P}_{ML,n_F}; \hat{\mathcal{P}}_{HP})], \quad (25)$$

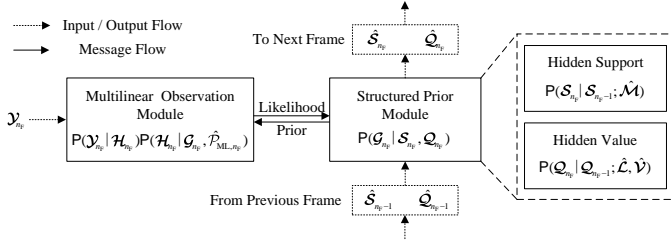


Fig. 5. Module diagram of the TS-DCP algorithm.

$$V_{b_{HG,n_F}}\{\mathcal{G}_{n_F}\} = V_{b_{G,n_F}}\{\mathcal{G}_{n_F}\} = V_{f_{G,n_F}}\{\mathcal{G}_{n_F}\}. \quad (30d)$$

Building upon the above BFE construction and MCC relaxation, the inference in the MO module is formulated as the constrained BFE minimization problem, given by

$$\arg \min_{\mathbf{b}_{MO,n_F}} F_{MO,n_F}, \quad \text{s.t. (30)}. \quad (31)$$

The constrained BFE minimization problem can be solved by the Lagrange multiplier method [52]. The Lagrange function is expressed as

$$L_{MO,n_F} = F_{MO,n_F} + L_{MO-FO,n_F} + L_{MO-SO,n_F}, \quad (32)$$

where L_{MO-FO,n_F} and L_{MO-SO,n_F} are the subfunctions of FO-SSCCs and SO-SSCCs defined in (33a) and (33b) at the top of the next page, respectively, $\mathcal{U}_{n_F}^{H,bHG}$, $\mathcal{U}_{n_F}^{H,bH}$, $\mathcal{U}_{n_F}^{G,bG}$ and $\mathcal{U}_{n_F}^{G,bHG}$ denote the Lagrange multipliers for FO-SSCCs, $\mathcal{E}_{n_F}^{H,bHG}$, $\mathcal{E}_{n_F}^{H,bH}$, $\mathcal{E}_{n_F}^{G,bG}$ and $\mathcal{E}_{n_F}^{G,bHG}$ denote the Lagrange multipliers for SO-SSCCs.

By setting the derivative of the Lagrangian function with respect to the beliefs to zero, and substituting the stationary points of the beliefs into FO-SSCCs and SO-SSCCs, the iteration equations for the Lagrange multipliers can be derived. These equations are organized based on the message flow backward and forward from the observation to the angle-delay-Doppler domain channel, summarized in Algorithm 1.

2) *SP Module*: In this module, due to correlations between elements in the hidden support tensor, the structured trial beliefs are still constructed by the Bethe method, given by

$$\mathbf{b}_{HS,n_F} = \frac{\mathbf{b}_{S,n_F}^{\text{lik}} \mathbf{b}_{S,n_F}^{\text{MRF}} \mathbf{b}_{S,n_F}^{\text{TC}}}{f_{S,n_F}^{F+1}}, \quad (34)$$

where $\mathbf{b}_{S,n_F}^{\text{lik}}$, $\mathbf{b}_{S,n_F}^{\text{MRF}}$, $\mathbf{b}_{S,n_F}^{\text{TC}}$ and f_{S,n_F} are introduced for likelihood PDF, MRF model, long-timescale correlation model, and \mathcal{S}_{n_F} , respectively, F denotes the number of elements in the action region. Therefore, the VFE of hidden support tensors in the SP module is expressed as

$$F_{HS,n_F} = D[\mathbf{b}_{S,n_F}^{\text{lik}} \parallel P_{\text{lik}}(\mathcal{S}_{n_F})] + D[\mathbf{b}_{S,n_F}^{\text{MRF}} \parallel P_{\text{MRF}}(\mathcal{S}_{n_F})] + D[\mathbf{b}_{S,n_F}^{\text{TC}} \parallel P_{\text{TC}}^{\text{OL}}(\mathcal{S}_{n_F}; \hat{\mathcal{M}})] + (F+1)H[f_{S,n_F}], \quad (35)$$

Algorithm 1 MO Module Iterative Procedure

Input:

- \mathcal{Y}_{n_F} : Observation tensor.
- $P_{\text{pri}}(\mathcal{G}_{n_F})$: Message of \mathcal{G}_{n_F} from SP module.
- $\hat{\mathcal{P}}_{ML,n_F}$: Estimation result of \mathcal{P}_{ML,n_F} .
- σ_z^2 : Noise variance

Output:

- $P_{\text{lik}}(\mathcal{G}_{n_F})$: Message of \mathcal{G}_{n_F} to SP module.
- $\hat{\mathcal{G}}_{n_F}$: Estimation result of \mathcal{G}_{n_F} .
- 1: $\mathcal{E}_{n_F}^{G,bHG} = (V_{b_{G,n_F}}\{\mathcal{G}_{n_F}\})^{\odot -2} - \mathcal{E}_{n_F}^{G,bG}/N$
- 2: $\mathcal{E}_{n_F}^{H,bH} = ((\mathcal{E}_{n_F}^{G,bHG})^{\odot -1} \times_1 |\tilde{\mathbf{A}}_h(\hat{\theta}_{n_F})|^{\odot 2} \times_2 |\tilde{\mathbf{A}}_v(\hat{\phi}_{n_F})|^{\odot 2} \times_3 |\tilde{\mathbf{B}}(\hat{\tau}_{n_F})|^{\odot 2} \times_4 |\tilde{\mathbf{C}}(\hat{\nu}_{n_F})|^{\odot 2})^{\odot -1}$
- 3: $\mathcal{N}_{n_F}^{H,bH} = -\mathcal{U}_{n_F}^{H,bH} \odot \mathcal{E}_{n_F}^{H,bH} + \hat{\mathcal{G}}_{n_F} \times_1 \tilde{\mathbf{A}}_h(\hat{\theta}_{n_F}) \times_2 \tilde{\mathbf{A}}_v(\hat{\phi}_{n_F}) \times_3 \tilde{\mathbf{B}}_{n_F}(\hat{\tau}_{n_F}) \times_4 \tilde{\mathbf{C}}_{n_F}(\hat{\nu}_{n_F})$
- 4: $P_{\text{pri}}(\mathcal{H}_{n_F}) = \text{CN}(\mathcal{H}_{n_F}; \mathcal{N}_{n_F}^{H,bH}, (\mathcal{E}_{n_F}^{H,bH})^{\odot -1})$
- 5: $\mathbf{b}_{H,n_F} \propto P(\mathcal{Y}_{n_F} \mid \mathcal{H}_{n_F}) P_{\text{pri}}(\mathcal{H}_{n_F}), \mathcal{H}_{n_F} = E_{\mathbf{b}_{H,n_F}}\{\mathcal{H}_{n_F}\}$
- 6: $\mathcal{E}_{n_F}^{H,bHG} = (V_{\mathbf{b}_{H,n_F}}\{\mathcal{H}_{n_F}\})^{\odot -2} - \mathcal{E}_{n_F}^{H,bH}$
- 7: $\Delta \mathcal{N}_{n_F} = \mathcal{U}_{n_F}^{H,bH} \odot \mathcal{E}_{n_F}^{H,bHG} + \hat{\mathcal{H}}_{n_F} - \mathcal{N}_{n_F}^{H,bH}$
- 8: $\mathcal{U}_{n_F}^{H,bH} = \Delta \mathcal{N}_{n_F} \odot ((\mathcal{E}_{n_F}^{H,bH})^{\odot -1} + (\mathcal{E}_{n_F}^{H,bHG})^{\odot -1})$
- 9: $\mathcal{J}_{n_F}^{H,bH} = \mathcal{E}_{n_F}^{H,bH} \odot (1 + \mathcal{E}_{n_F}^{H,bH} \odot (V_{\mathbf{b}_{H,n_F}}\{\mathcal{H}_{n_F}\})^{\odot 2})$
- 10: $\mathcal{J}_{n_F}^{G,bG} = \mathcal{J}_{n_F}^{H,bH} \times_1 |\tilde{\mathbf{A}}_h(\hat{\theta}_{n_F})|^{\odot 2} \times_2 |\tilde{\mathbf{A}}_v(\hat{\phi}_{n_F})|^{\odot 2} \times_3 |\tilde{\mathbf{B}}(\hat{\tau}_{n_F})|^{\odot 2} \times_4 |\tilde{\mathbf{C}}(\hat{\nu}_{n_F})|^{\odot 2}$
- 11: $\mathcal{E}_{n_F}^{G,bG} = ((\mathcal{J}_{n_F}^{G,bG})^{\odot -1} - (N \mathcal{E}_{n_F}^{H,bHG})^{\odot -1})^{\odot -1}$
- 12: $\mathcal{N}_{n_F}^{G,bG} = \hat{\mathcal{G}}_{n_F} + (\mathcal{E}_{n_F}^{G,bG})^{\odot -1} \odot (\mathcal{U}_t^{R,bR} \times_1 \hat{\mathbf{A}}_h^H(\hat{\theta}_{n_F}) \times_2 \hat{\mathbf{A}}_v^H(\hat{\phi}_{n_F}) \times_3 \tilde{\mathbf{B}}^H(\hat{\tau}_{n_F}) \times_4 \tilde{\mathbf{C}}^H(\hat{\nu}_{n_F}))$
- 13: $P_{\text{lik}}(\mathcal{G}_{n_F}) = \text{CN}(\mathcal{G}_{n_F}; \mathcal{N}_{n_F}^{G,bG}, (\mathcal{E}_{n_F}^{G,bG})^{\odot -1})$
- 14: $\mathbf{b}_{G,n_F} \propto P_{\text{pri}}(\mathcal{G}_{n_F}) P_{\text{lik}}(\mathcal{G}_{n_F}), \hat{\mathcal{G}}_{n_F} = E_{\mathbf{b}_{G,n_F}}\{\mathcal{G}_{n_F}\}$

where $P_{\text{lik}}(\mathcal{S}_{n_F})$ and $P_{\text{TC}}^{\text{OL}}(\mathcal{S}_{n_F}; \hat{\mathcal{M}})$ denote the likelihood PDF and temporal correlation model with an online approximation of hidden support tensors, respectively, and we define $P_{\text{TC}}^{\text{OL}}(\mathcal{S}_{n_F}; \hat{\mathcal{M}}) \triangleq P_{\text{TC}}(\mathcal{S}_{n_F} \mid \mathcal{S}_{n_F-1}; \hat{\mathcal{M}})$. Furthermore, since the elements in the hidden support tensor are binary-valued, the MCCs are equivalent to FO-SSCCs, given by

$$E_{\mathbf{b}_{S,n_F}^{(d,k)}}\{\mathcal{S}_{n_F}\} = E_{\mathbf{b}_{S,n_F}^{\text{TC}}}\{\mathcal{S}_{n_F}\} = E_{\mathbf{b}_{S,n_F}^{\text{lik}}}\{\mathcal{S}_{n_F}\} = E_{f_{S,n_F}}\{\mathcal{S}_{n_F}\}, \quad (36)$$

where $\mathbf{b}_{S,n_F}^{(d,k)}$ denotes the factor belief of MRFs in action dimension d and action step k , given by

$$\mathbf{b}_{S,n_F}^{\text{MRF}}(\mathcal{S}_{n_F}) = \prod_{(d,k) \in \mathcal{N}} \mathbf{b}_{S,n_F}^{(d,k)}(\mathcal{S}_{n_F}, \mathcal{S}_{n_F}^{(d,k)}). \quad (37)$$

Building upon the above BFE construction and MCCs, the Lagrange function of VFE minimization in the SP module is expressed as

$$L_{HS,n_F} = F_{HS,n_F} + L_{MCC,n_F}, \quad (38)$$

$$L_{\text{MO-FO},n_F} = 2\text{Re}\{\langle \mathbf{U}_{n_F}^{H,bHG}, [\mathbf{E}_{b_{Y,n_F}}\{\mathcal{H}_{n_F}\} - \mathbf{E}_{f_{H,n_F}}\{\mathcal{H}_{n_F}\}] \rangle + \langle \mathbf{U}_{n_F}^{H,bH}, [\mathbf{E}_{b_{HG,n_F}}\{\mathcal{H}_{n_F}\} - \mathbf{E}_{f_{H,n_F}}\{\mathcal{H}_{n_F}\}] \rangle + \langle \mathbf{U}_{n_F}^{G,bG}, [\mathbf{E}_{b_{G,n_F}}\{\mathcal{G}_{n_F}\} - \mathbf{E}_{f_{G,n_F}}\{\mathcal{G}_{n_F}\}] \rangle + \langle \mathbf{U}_{n_F}^{G,bHG}, [\mathbf{E}_{b_{HG,n_F}}\{\mathcal{G}_{n_F}\} - \mathbf{E}_{f_{G,n_F}}\{\mathcal{G}_{n_F}\}] \rangle\}, \quad (33a)$$

$$L_{\text{MO-SO},n_F} = \langle \mathcal{E}_{n_F}^{H,bHG}, [\mathbf{V}_{b_{Y,n_F}}\{\mathcal{H}_{n_F}\} - \mathbf{V}_{f_{H,n_F}}\{\mathcal{H}_{n_F}\}] \rangle + \langle \mathcal{E}_{n_F}^{H,bH}, [\mathbf{V}_{b_{HG,n_F}}\{\mathcal{H}_{n_F}\} - \mathbf{V}_{f_{H,n_F}}\{\mathcal{H}_{n_F}\}] \rangle + \langle \mathcal{E}_{n_F}^{G,bG}, [\mathbf{V}_{b_{G,n_F}}\{\mathcal{G}_{n_F}\} - \mathbf{V}_{f_{G,n_F}}\{\mathcal{G}_{n_F}\}] \rangle + \langle \mathcal{E}_{n_F}^{G,bHG}, [\mathbf{V}_{b_{HG,n_F}}\{\mathcal{G}_{n_F}\} - \mathbf{V}_{f_{G,n_F}}\{\mathcal{G}_{n_F}\}] \rangle. \quad (33b)$$

Algorithm 2 SP Module Iterative Procedure

Input:

- $P_{\text{lik}}(\mathcal{S}_{n_F})$: Message of \mathcal{S}_{n_F} from MO module.
- $P_{\text{lik}}(\mathcal{Q}_{n_F})$: Message of \mathcal{Q}_{n_F} from MO module.
- $\hat{\mathcal{P}}_{\text{HP}}$: Estimation result of \mathcal{P}_{HP} .

Output:

- $P_{\text{pri}}(\mathcal{S}_{n_F})$: Message of \mathcal{S}_{n_F} to MO module.
- $P_{\text{pri}}(\mathcal{Q}_{n_F})$: Message of \mathcal{Q}_{n_F} to MO module.
- 1: $\bar{\mathbf{u}}_{n_F}^{\text{MRF}}(d,k) = \sum_{(\bar{d},\bar{k}) \in \mathcal{N} \setminus (d,k)} \mathbf{u}_{n_F}^{\text{MRF}}(\bar{d},\bar{k}), \forall (d,k)$
- 2: $\mathbf{u}_{n_F}^{S,\text{MRF}}(d,k) = \mathbf{u}_{n_F}^{\text{lik}} + \mathbf{u}_{n_F}^{\text{TC}} + \bar{\mathbf{u}}_{n_F}^{\text{MRF}}(d,k), \forall (d,k)$
- 3: $\mathbf{u}_{n_F}^{\text{MRF},1}(d,k) = 1 + \exp(2C_S + \mathbf{u}_{n_F}^{S,\text{MRF}}(d,k)), \forall (d,k)$
- 4: $\mathbf{u}_{n_F}^{\text{MRF},2}(d,k) = \exp(2C_S) + \exp(\mathbf{u}_{n_F}^{S,\text{MRF}}(d,k)), \forall (d,k)$
- 5: $\mathbf{u}_{n_F}^{\text{MRF}}(d,k) = \mathbf{u}_{n_F}^{\text{MRF},1}(d,k) - \mathbf{u}_{n_F}^{\text{MRF},2}(d,k), \forall (d,k)$
- 6: $\mathbf{u}_{n_F}^{\text{MRF}} = \sum_{(d,k) \in \mathcal{N}} \mathbf{u}_{n_F}^{\text{MRF}}(d,k), \forall (d,k)$
- 7: $P_{\text{pri}}(\mathcal{S}_{n_F}) = \exp(-\langle \mathbf{u}_{n_F}^{\text{TC}} + \mathbf{u}_{n_F}^{\text{MRF}}, \mathcal{S}_{n_F} \rangle)$
- 8: $\mathbf{b}_{S,n_F} \propto P_{\text{lik}}(\mathcal{S}_{n_F})P_{\text{pri}}(\mathcal{S}_{n_F}), \mathbf{b}_{Q,n_F} \propto P_{\text{lik}}(\mathcal{Q}_{n_F})P_{\text{pri}}(\mathcal{Q}_{n_F})$
- 9: $\hat{\mathcal{S}}_{n_F} = \text{Id}(\mathbf{E}_{b_{S,n_F}}\{\mathcal{S}_{n_F}\} > \text{Th}), \hat{\mathcal{Q}}_{n_F} = \mathbf{E}_{b_{Q,n_F}}\{\mathcal{Q}_{n_F}\}$

where L_{MCC,n_F} is defined as

$$L_{\text{MCC},n_F} = \langle \mathbf{u}_{n_F}^{S,\text{lik}}, [\mathbf{E}_{b_{S,n_F}^{\text{lik}}}\{\mathcal{S}_{n_F}\} - \mathbf{E}_{f_{S,n_F}}\{\mathcal{S}_{n_F}\}] \rangle + \sum_{(d,k) \in \mathcal{N}} \langle \mathbf{u}_{n_F}^{S,\text{MRF}}(d,k), [\mathbf{E}_{b_{S,n_F}^{(d,k)}}\{\mathcal{S}_{n_F}\} - \mathbf{E}_{f_{S,n_F}}\{\mathcal{S}_{n_F}\}] \rangle + \langle \mathbf{u}_{n_F}^{S,\text{TC}}, [\mathbf{E}_{b_{S,n_F}^{\text{TC}}}\{\mathcal{S}_{n_F}\} - \mathbf{E}_{f_{S,n_F}}\{\mathcal{S}_{n_F}\}] \rangle, \quad (39)$$

where $\mathbf{u}_{n_F}^{S,\text{lik}}, \mathbf{u}_{n_F}^{S,\text{MRF}}$ and $\mathbf{u}_{n_F}^{S,\text{TC}}$ denote the Lagrange multipliers for MCCs.

Since the elements of \mathcal{Q}_{n_F} are conditionally independent given $\hat{\mathcal{Q}}_{n_F-1}, \mathcal{L}$ and \mathcal{V} , the structured trial beliefs need only be constrained to exponential family, guaranteeing the tractability of VFE minimization. Therefore, the inference of hidden value tensors in the SP module is expressed as

$$\arg \min_{\mathbf{b}_{\text{HV},n_F}} D[\mathbf{b}_{Q,n_F} \parallel P_{\text{lik}}(\mathcal{Q}_{n_F})P_{\text{TC}}^{\text{OL}}(\mathcal{Q}_{n_F}; \hat{\mathcal{L}}, \hat{\mathcal{V}})], \quad (40)$$

where $P_{\text{lik}}(\mathcal{Q}_{n_F})$ and $P_{\text{TC}}^{\text{OL}}(\mathcal{Q}_{n_F}; \hat{\mathcal{L}}, \hat{\mathcal{V}})$ denote the likelihood PDF and the temporal correlation model with online approximation of hidden value tensors, respectively, and we define $P_{\text{TC}}^{\text{OL}}(\mathcal{Q}_{n_F}; \hat{\mathcal{L}}, \hat{\mathcal{V}}) \triangleq P(\mathcal{Q}_{n_F} \mid \hat{\mathcal{Q}}_{n_F-1}; \hat{\mathcal{L}}, \hat{\mathcal{V}})$.

By substituting the stationary points derived from the Lagrangian function into the MCCs, the equations are organized based on the message flow and summarized in Algorithm 2. In this context, $\mathbf{u}_{n_F}^{\text{lik}}$ and $\mathbf{u}_{n_F}^{\text{TC}}$ denote the log-likelihood ratio of $P_{\text{lik}}(\mathcal{S}_{n_F})$ and $P_{\text{TC}}^{\text{OL}}(\mathcal{S}_{n_F})$, respectively.

3) *Online TS-DCP Algorithm*: In the MO and SP modules, the prior PDFs of the angle-delay-Doppler domain channel tensor $P_{\text{pri}}(\mathcal{G}_{n_F})$, the likelihood PDFs of the hidden support tensor $P_{\text{lik}}(\mathcal{S}_{n_F})$, and the likelihood PDFs of the hidden values tensor $P_{\text{lik}}(\mathcal{Q}_{n_F})$ remain undefined. These PDFs are crucial for information exchange between the modules and for the development of the online TS-DCP algorithm.

Based on the joint PDF factorization and the stationary point of beliefs, the joint posterior PDF of $\mathcal{G}_{n_F}, \mathcal{S}_{n_F}$ and \mathcal{Q}_{n_F} is

$$P(\mathcal{G}_{n_F}, \mathcal{S}_{n_F}, \mathcal{Q}_{n_F} \mid \mathcal{Y}_{n_F}) \propto P(\mathcal{G}_{n_F} \mid \mathcal{S}_{n_F}, \mathcal{Q}_{n_F})P_{\text{pri}}(\mathcal{S}_{n_F})P_{\text{lik}}(\mathcal{G}_{n_F})P_{\text{pri}}(\mathcal{Q}_{n_F}). \quad (41)$$

Therefore, the prior and likelihood PDFs are obtained by marginalizing the joint posterior PDF and excluding the contributions of the input data. Notably, the zero elements in \mathcal{S}_{n_F} result in the unobservability of the corresponding elements in \mathcal{Q}_{n_F} , thus yielding the uninformative likelihood PDFs and preventing the VFE minimization. To mitigate this issue, we adopt the threshold-based Gaussian sum approximation [48] in the likelihood PDF of \mathcal{Q}_{n_F} .

With the rules for updating prior and likelihood PDFs, along with Algorithm 1 and Algorithm 2, the online TS-DCP algorithm is summarized as Algorithm 3, where hyperparameter and generator learning are discussed in the next subsection. It is important to note that Doppler domain based short-timescale correlation modeling allows the prediction of data segment channels without additional reference signals. To avoid large delays caused by the collection of pilot OFDM symbols, we employ Algorithm 3 based on sliding windows instead of frames. This approach enables dynamic frame reorganization as new pilot OFDM symbols become available, facilitating real-time channel prediction.

B. Generator and Hyperparameter Learning

1) *Generator Learning*: To reduce the search space of varying generators, rather than estimating the generators $\hat{\mathcal{P}}_{\text{ML},n_F}$ directly using unconstrained approaches, we estimate the difference between the ground-truth generators and the previous generator learning results, expressed as

$$\Delta \chi_{n_F} = \hat{\chi}_{n_F} - \hat{\chi}_{n_F}^{\text{P}}, \quad (42)$$

where $\hat{\chi}_{n_F}^{\text{P}}$ denotes the previous generator learning result and $\chi \in \{\theta, \phi, \tau, \nu\}$. To reduce computational complexity, we optimize the generators sequentially, alternating between them rather than optimizing them jointly. In the example of the

Algorithm 3 Online TS-DCP Algorithm

Input:

$\mathcal{Y}_{(N_F)}$: Observation tensor.
 σ_z^2 : Noise variance

Output:

$\hat{\mathcal{G}}_{(N_F)}$: Estimation result of $\mathcal{G}_{(N_F)}$.

$\hat{\mathcal{P}}_{ML,(N_F)}$: Estimation result of $\mathcal{P}_{ML,(N_F)}$.

- 1: Initialize the hyperparameters $\hat{\mathcal{M}}$, $\hat{\mathcal{L}}$ and $\hat{\mathcal{V}}$.
 - 2: Set the initial state $\hat{\mathcal{S}}_0 = 0$ and $\hat{\mathcal{Q}}_0 = 0$.
 - 3: **for** $n_F = 1, \dots, N_F$ **do**
 - 4: **for** $t = 1 : T$ **do**
 - 5: Obtain the prior PDF of \mathcal{G}_{n_F} .
 - 6: Execute Algorithm 1.
 - 7: Obtain the likelihood PDFs of \mathcal{S}_{n_F} and \mathcal{Q}_{n_F} .
 - 8: Execute Algorithm 2.
 - 9: Generator and hyperparameter learning.
 - 10: **end for**
 - 11: **end for**
-

horizontal angle domain, the generator learning rule based on the VFE minimization is formulated as

$$\begin{aligned} \Delta\theta_{n_F}^* &\stackrel{(a)}{=} \arg \min_{\Delta\theta_{n_F}} D[\mathbf{b}_{HG,n_F} \parallel \mathbf{P}(\mathcal{H}_{n_F} | \mathcal{G}_{n_F}, \hat{\mathcal{P}}_{\setminus h,n_F})] \\ &= \arg \max_{\Delta\theta_{n_F}} \underbrace{\int \mathbf{b}_{HG,n_F} \ln \mathbf{P}(\mathcal{H}_{n_F} | \mathcal{G}_{n_F}; \hat{\mathcal{P}}_{\setminus h,n_F})}_{\triangleq f(\Delta\theta_{n_F})}, \end{aligned} \quad (43)$$

where (a) is due to only this KL divergence term depending on $\Delta\theta_{n_F}$, $\hat{\mathcal{P}}_{\setminus h,n_F} \triangleq \{\hat{\theta}_{n_F}^p + \Delta\theta_{n_F}, \hat{\phi}_{n_F}^p, \hat{\tau}_{n_F}^p, \hat{\nu}_{n_F}^p\}$ consists of the horizontal angle currently being optimized and the previously optimized results from other domains. Due to the singularity in Dirac Delta functions, the conditional PDF $\mathbf{P}(\mathcal{H}_{n_F} | \mathcal{G}_{n_F}; \hat{\mathcal{P}}_{\setminus h,n_F})$ is approximated by (45) at the top of the next page. On this basis, the objective function for horizontal angle domain generator learning rule is expressed as

$$f(\Delta\theta_{n_F}) = f_1(\Delta\theta_{n_F}) + f_2(\Delta\theta_{n_F}), \quad (44)$$

where $f_1(\Delta\theta_{n_F})$ and $f_2(\Delta\theta_{n_F})$ denote the objective subfunction, defined by (46) at the top of the next page.

The structured factor matrix $\tilde{\mathbf{A}}_h(\hat{\theta}_{n_F}^p + \Delta\theta_{n_F})$ is approximated by the first-order Taylor series, given by

$$\tilde{\mathbf{A}}_h(\hat{\theta}_{n_F}^p + \Delta\theta_{n_F}) \approx \tilde{\mathbf{A}}_h(\hat{\theta}_{n_F}^p) + \dot{\mathbf{A}}_h(\hat{\theta}_{n_F}^p) \text{diag}\{\Delta\theta_{n_F}\}, \quad (47)$$

where $\dot{\mathbf{A}}_h(\cdot)$ denotes the derivative matrix of the horizontal angle domain structured factor matrix with respect to the horizontal direction cosine. Based on the Taylor approximation and the commutativity of tensor-matrix multiplication across dimensions, the first subfunction $f_1(\Delta\theta_{n_F})$ is expressed as

$$\begin{aligned} f_1(\Delta\theta_{n_F}) &= \|\Delta\hat{\mathcal{H}}_{n_F} - \hat{\mathcal{G}}_{n_F}^h \times_1 \dot{\mathbf{A}}_h(\hat{\theta}_{n_F}^p) \text{diag}\{\Delta\theta_{n_F}\}\|_F^2 \\ &= \sum_n \|\Delta\hat{\mathbf{h}}_{n_F,n}^{(1)} - \dot{\mathbf{A}}_h(\hat{\theta}_{n_F}^p) \text{diag}\{\mathbf{g}_{n_F,n}^h\} \Delta\theta_{n_F}\|_F^2 \\ &= \Delta\theta_{n_F}^T \mathbf{\Pi}_{h,1} \Delta\theta_{n_F} - 2\mu_{h,1}^T \Delta\theta_{n_F} + C_1, \end{aligned} \quad (48)$$

where $\Delta\hat{\mathcal{H}}_{n_F}$ denotes the residual tensor of spatial-frequency-temporal domain channel, given by

$$\begin{aligned} \Delta\hat{\mathcal{H}}_{n_F} &= \hat{\mathcal{H}}_{n_F} - \hat{\mathcal{G}}_{n_F} \times_1 \tilde{\mathbf{A}}_h(\hat{\theta}_{n_F}^p) \times_2 \tilde{\mathbf{A}}_v(\hat{\phi}_{n_F}^p) \\ &\quad \times_3 \tilde{\mathbf{B}}_{n_F}(\hat{\tau}_{n_F}^p) \times_4 \tilde{\mathbf{C}}(\hat{\nu}_{n_F}^p), \end{aligned} \quad (49)$$

$\hat{\mathcal{G}}_{n_F}^h = \hat{\mathcal{G}}_{n_F} \times_2 \tilde{\mathbf{A}}_v(\hat{\phi}_{n_F}^p) \times_3 \tilde{\mathbf{B}}_{n_F}(\hat{\tau}_{n_F}^p) \times_4 \tilde{\mathbf{C}}(\hat{\nu}_{n_F}^p)$ denotes the multilinear transformation of $\hat{\mathcal{G}}_{n_F}$ without the horizontal angle domain, $\Delta\hat{\mathbf{h}}_{n_F,n}$ and $\mathbf{g}_{n_F,n}^h$ denote the fibers of $\Delta\hat{\mathcal{H}}_{n_F}$ and $\hat{\mathcal{G}}_{n_F}^h$ with respect to the first dimension, respectively, C_1 denotes the term unrelated to $\Delta\theta_{n_F}$, $\mathbf{\Pi}_{h,1}$ and $\mu_{h,1}$ denote the auxiliary matrix and vector, given by

$$\mathbf{\Pi}_{h,1} = (\dot{\mathbf{A}}_h^H(\hat{\theta}_{n_F}^p) \dot{\mathbf{A}}_h(\hat{\theta}_{n_F}^p))^* \odot \hat{\mathbf{G}}_{n_F}^h (\hat{\mathbf{G}}_{n_F}^h)^H, \quad (50a)$$

$$\mu_{h,1} = \sum_n \text{Re}\{\text{diag}^H\{\mathbf{g}_{n_F,n}^h\} \dot{\mathbf{A}}_h^H(\hat{\theta}_{n_F}^p) \Delta\hat{\mathbf{h}}_{n_F,n}^{(1)}\}. \quad (50b)$$

Similarly, the second subfunction $f_2(\Delta\theta_{n_F})$ is expressed as

$$\begin{aligned} f_2(\Delta\theta_{n_F}) &= \|\mathcal{E}_{G,n_F}^h \times_1 |\tilde{\mathbf{A}}_h(\hat{\theta}_{n_F}^p + \Delta\theta_{n_F})|^{\odot 2}\|_1 \\ &= \sum_n \|\tilde{\mathbf{A}}_h(\hat{\theta}_{n_F}^p + \Delta\theta_{n_F})|^{\odot 2} \mathbf{e}_{G,n_F,n}^h\|_1 \\ &= \Delta\theta_{n_F}^T \mathbf{\Pi}_{h,2} \Delta\theta_{n_F} - 2\mu_{h,2}^T \Delta\theta_{n_F} + C_2, \end{aligned} \quad (51)$$

where \mathcal{E}_{G,n_F}^h denotes the multilinear transformation of \mathcal{E}_{G,n_F} without the horizontal angle domain, given by

$$\begin{aligned} \mathcal{E}_{G,n_F}^h &\triangleq \mathcal{E}_{G,n_F} \times_2 |\tilde{\mathbf{A}}_v(\hat{\phi}_{n_F}^p)|^{\odot 2} \\ &\quad \times_3 |\tilde{\mathbf{B}}(\hat{\tau}_{n_F}^p)|^{\odot 2} \times_4 |\tilde{\mathbf{C}}(\hat{\nu}_{n_F}^p)|^{\odot 2}, \end{aligned} \quad (52)$$

$\mathbf{e}_{G,n_F,n}^h$ denotes the fiber of \mathcal{E}_{G,n_F}^h with respect to the first dimension, C_2 denotes the term unrelated to $\Delta\theta_{n_F}$, $\mathbf{\Pi}_{h,2}$ and $\mu_{h,2}$ denote the auxiliary matrix and vector, given by

$$\mathbf{\Pi}_{h,2} = (\dot{\mathbf{A}}_h^H(\hat{\theta}_{n_F}^p) \dot{\mathbf{A}}_h(\hat{\theta}_{n_F}^p))^* \odot \sum_n \text{diag}\{\mathbf{e}_{G,n_F,n}^h\}, \quad (53a)$$

$$\mu_{h,2} = -\text{Re}\{\text{diag}\{\dot{\mathbf{A}}_h^H(\hat{\theta}_{n_F}^p) \tilde{\mathbf{A}}_h(\hat{\theta}_{n_F}^p)\} \odot \sum_n \mathbf{e}_{G,n_F,n}^h\}. \quad (53b)$$

On this basis, the objective function for horizontal angle domain generator learning is expressed as

$$f(\Delta\theta_{n_F}) = \Delta\theta_{n_F}^T \mathbf{\Pi}_h \Delta\theta_{n_F} - 2\mu_h^T \Delta\theta_{n_F} + C, \quad (54)$$

where $\mathbf{\Pi}_h = \mathbf{\Pi}_{h,1} + \mathbf{\Pi}_{h,2}$, $\mu_h = \mu_{h,1} + \mu_{h,2}$ and $C = C_1 + C_2$. The generator learning rules in other domains are formulated similarly, which allows for addressing them with low complexity. By leveraging efficient tensor operations, the auxiliary matrices and vectors in the quadratic optimization problems are also constructed in a manner that significantly reduces computational complexity.

2) *Hyperparameter Learning*: Different from the generators, the hyperparameters in \mathcal{P}_{HP} are shared across all frames and learned adaptively based on observations in the current frame. For the N_F -th frame, the hyperparameter learning rules based on the VFE minimization are expressed as

$$\hat{\mathcal{M}}^* = \arg \max_{\hat{\mathcal{M}}} \sum_{n_F=1}^{N_F} \int \mathbf{b}_{S,n_F} \ln \mathbf{P}(\mathcal{S}_{n_F} | \mathcal{S}_{n_F-1}; \hat{\mathcal{M}}), \quad (55a)$$

$$P(\mathcal{H}_{n_F} | \mathcal{G}_{n_F}; \hat{\mathcal{P}}_{\setminus h, n_F}) \approx \lim_{\epsilon \rightarrow 0} \text{CN}(\mathcal{H}_{n_F}; \hat{\mathcal{G}}_{n_F} \times_1 \tilde{\mathbf{A}}_h(\hat{\boldsymbol{\theta}}_{n_F}^p + \Delta \boldsymbol{\theta}_{n_F}) \times_2 \tilde{\mathbf{A}}_v(\hat{\boldsymbol{\phi}}_{n_F}^p) \times_3 \tilde{\mathbf{B}}_{n_F}(\hat{\boldsymbol{\tau}}_{n_F}^p) \times_4 \tilde{\mathbf{C}}(\hat{\boldsymbol{\nu}}_{n_F}^p), \mathcal{C}(\epsilon)). \quad (45)$$

$$f_1(\Delta \boldsymbol{\theta}_{n_F}) = \|\hat{\mathcal{H}}_{n_F} - \hat{\mathcal{G}}_{n_F} \times_1 \tilde{\mathbf{A}}_h(\hat{\boldsymbol{\theta}}_{n_F}^p + \Delta \boldsymbol{\theta}_{n_F}) \times_2 \tilde{\mathbf{A}}_v(\hat{\boldsymbol{\phi}}_{n_F}^p) \times_3 \tilde{\mathbf{B}}_{n_F}(\hat{\boldsymbol{\tau}}_{n_F}^p) \times_4 \tilde{\mathbf{C}}(\hat{\boldsymbol{\nu}}_{n_F}^p)\|_F^2, \quad (46a)$$

$$f_2(\Delta \boldsymbol{\theta}_{n_F}) = \|\mathcal{E}_{G, n_F} \times_1 |\tilde{\mathbf{A}}_h(\hat{\boldsymbol{\theta}}_{n_F}^p + \Delta \boldsymbol{\theta}_{n_F})|^{\odot 2} \times_2 |\tilde{\mathbf{A}}_v(\hat{\boldsymbol{\phi}}_{n_F}^p)|^{\odot 2} \times_3 |\tilde{\mathbf{B}}(\hat{\boldsymbol{\tau}}_{n_F}^p)|^{\odot 2} \times_4 |\tilde{\mathbf{C}}(\hat{\boldsymbol{\nu}}_{n_F}^p)|^{\odot 2}\|_1, \quad (46b)$$

$$\{\hat{\mathcal{L}}^*, \hat{\mathcal{V}}^*\} = \arg \max_{\{\mathcal{L}, \mathcal{V}\}} \sum_{n_F=1}^{N_F} \int b_{Q, n_F} \ln P(\mathcal{Q}_{n_F} | \mathcal{Q}_{n_F-1}; \mathcal{L}, \mathcal{V}). \quad (55b)$$

The hyperparameter learning rule is derived by setting the derivatives of the objective function with respect to the hyperparameters to zero. Specifically, the learning rule of the transition factor hyperparameter in the hidden support tensor is expressed by

$$\hat{\mathcal{M}}^* = \ln(1 + \mathcal{K}_M) - \ln(1 - \mathcal{K}_M), \quad (56)$$

where \mathcal{K}_M denotes the auxiliary tensor, given by

$$\mathcal{K}_M = \frac{1}{N_F} \sum_{n_F=1}^{N_F} (2\mathcal{S}_{n_F} - 1) \odot (2\mathcal{S}_{n_F-1} - 1). \quad (57)$$

Besides, due to the coupling of hyperparameters in the hidden value tensor, finding an analytic solution for the optimal power variation hyperparameter is intractable. To address this issue, we first learn the equivalent power variation hyperparameter $\bar{\mathcal{V}}$ instead, with its learning rule given in (58) at the top of the next page. Based on the method in [53], [54], the sub-optimal power variation hyperparameter is given by

$$\hat{\mathcal{V}} = \bar{\mathcal{V}} + C_V \sum_{(d,k) \in \mathcal{N}} \bar{\mathcal{V}}^{(d,k)}. \quad (59)$$

For the optimal temporal correlation hyperparameter $\hat{\mathcal{L}}^*$, it satisfies the following quadratic equation

$$\mathcal{K}_{L,2} \|\hat{\mathcal{L}}^*\|^{\odot 2} + \mathcal{K}_{L,1} \hat{\mathcal{L}}^* + \mathcal{K}_{L,0} = 0, \quad (60)$$

where the coefficients $\mathcal{K}_{L,2}$, $\mathcal{K}_{L,1}$ and $\mathcal{K}_{L,0}$ are defined as

$$\mathcal{K}_{L,2} \triangleq (N_F - 1) \bar{\mathcal{V}}, \quad (61a)$$

$$\mathcal{K}_{L,1} \triangleq \sum_{n_F=2}^{N_F} (|\hat{\mathcal{Q}}_{n_F-1}|^{\odot 2} - \text{Re}\{\hat{\mathcal{Q}}_{n_F-1}^* \odot \hat{\mathcal{Q}}_{n_F}\}), \quad (61b)$$

$$\mathcal{K}_{L,0} \triangleq - \sum_{n_F=2}^{N_F} (|\hat{\mathcal{Q}}_{n_F} - \hat{\mathcal{Q}}_{n_F-1}|^{\odot 2} + \mathcal{E}_{Q, n_F}). \quad (61c)$$

Therefore, the transition factor, as well as the temporal correlation and power variation hyperparameters, can all be learned in an element-wise manner.

C. Computational Complexity Analysis

To generalize the computational complexity analysis, we define the order of the observation and core tensors as D , with the size of the d -th dimensions denoted by N_d and K_d , respectively. For scalar operations in Algorithm 2 and hyperparameter learning, the computational complexity depends

on the size of the core tensor, resulting in $\mathcal{O}(\prod_{d=1}^D K_d)$. On the other hand, for tensor-matrix multiplications in Algorithm 1 and generator learning, the complexity is significantly impacted by the order in which the multiplications are executed, due to the commutative property of tensor-matrix operations. To account for this, the computational complexity is expressed as $\mathcal{O}(\min_{\pi} \sum_{m=1}^D \prod_{d=\pi(1)}^{\pi(m)} K_d \prod_{d=\pi(m)}^{\pi(D)} N_d)$, where π denotes the permutation vector of size D . Therefore, the computational complexity of Algorithm 3 is expressed as $\mathcal{O}(\min_{\pi} T \sum_{m=1}^D \prod_{d=\pi(1)}^{\pi(m)} K_d \prod_{d=\pi(m)}^{\pi(D)} N_d)$, where T denotes the number of iterations. Assuming the core tensor size is proportional to the observation tensor, as is common in practical systems, the computational complexity can be further simplified to $\mathcal{O}(T \sum_m N_m \prod_{d=1}^D N_d)$. This implies the reduction in computational complexity due to the multilinear structure, compared to the computational complexity of the unstructured method $\mathcal{O}(T \prod_{d=1}^D N_d^2)$.

VI. SIMULATION RESULTS

A. Simulation Configuration

In this section, we present simulation results to evaluate the channel prediction performance of the proposed algorithm. For this purpose, we employ the QuaDRiGa channel simulator, which generates massive MIMO-OFDM channels consistent with the third Generation Partnership Program (3GPP) New Radio (NR) specifications [55] and has been validated in various field trials [56]. In the QuaDRiGa channel simulator, we consider the 3GPP urban macro (UMa) non-line-of-sight (NLOS) scenarios, where each channel contains 20 clusters consisting of 20 subpaths with similar physical parameters. As mobile terminals (MTs) traverse their trajectory, the contribution of scatterers to the channel evolves with time and the spatial consistency of the channels is maintained. The carrier frequency f_c is set to 6.7 GHz in the upper mid-band, which is vital in future communications. Unless specified otherwise, the simulation configurations follow the system model in Section III, with parameters summarized in Table I.

B. Benchmarks and Performance Metric

To demonstrate the superiority of the proposed online TS-DCP algorithm, we select the following state-of-the-art algorithms as benchmarks:

- **VKF** [26]: Estimates spatial domain channels by the least square (LS) algorithm, with temporal correlations captured by the AR-based vector KF.
- **FIT** [31]: Estimates angle-delay domain channels by the alternating LS (ALS) algorithm, with temporal correlations captured by the first-order Taylor series.

$$\bar{\mathbf{V}} = \frac{1}{N_F} (|\hat{\mathbf{Q}}_1|^{\odot 2} + \mathcal{E}_{Q,1} + \sum_{n_F=2}^{N_F} (|\hat{\mathbf{Q}}_{n_F}|^{\odot 2} + \mathcal{E}_{Q,n_F} - 2(1 - \hat{\mathcal{L}}) \odot \text{Re}\{\hat{\mathbf{Q}}_{n_F-1}^* \odot \hat{\mathbf{Q}}_{n_F}\} + (1 - \hat{\mathcal{L}}) \odot |\hat{\mathbf{Q}}_{n_F-1}|^{\odot 2}) \oslash \hat{\mathcal{L}}^{\odot 2}) \quad (58)$$

TABLE I
SCENARIO PARAMETERS

Paramter	Value
Carrier Frequency	$f_c = 6.7$ GHz
Pilot Symbol Interval	$\Delta T = 14 \times 35.68$ μ s
Pilot Subcarrier Spacing	$\Delta f = 4 \times 30$ kHz
Number of BS Antennas	$(N_h, N_v) = (32, 16)$
Number of Pilot Subcarriers	$N_{sc} = 64$
Number of Pilot Symbols	$N_{sym} = 8$
Height of BS	$h_{BS} = 25$ m
Height of MTs	$h_{MT} = 1.5$ m
MT Distribution Radius	$r_{MT} = 200$ m

- **PAD** [13]: Estimates angle-delay domain channels by the linear MMSE (LMMSE) algorithm, with temporal correlations captured by the Prony method.

Besides, we include **Online TS-DCP** algorithm with pre-sampled generators and unstructured independent prior as benchmarks, referred to as **Online TS-DCP (PG)** and **Online TS-DCP (UIP)**, respectively. For performance comparison, the time-averaged normalized mean square error (TNMSE) of the spatial-frequency domain channels is adopted as the metric. Since both **VKF** and **PAD** predict channels only for future pilot symbols, we predict channels on non-pilot symbols through MMSE interpolation, with prior knowledge of the maximum Doppler frequency and transmission power [57].

C. Performance Evaluation

1) *TNMSE for Different Transmission Power*: The TNMSE of the proposed algorithm and benchmarks versus transmission power for $v = 60$ km/h and $v = 120$ km/h are shown in Fig. 6. It is clear that the proposed algorithms significantly outperform the benchmarks across the full transmission power range. Since the fundamental limitation of **FIT** is the dependence on the ALS algorithm, **FIT** struggles to incorporate statistical CSI and noise variance, resulting in a noticeable performance drop in the low transmission power regime. Furthermore, **FIT** fails to achieve a TNMSE below 0 dB at $v = 120$ km/h due to the inaccuracy of the first-order Taylor series in modeling temporal correlations at high mobility. While **VKF** benefits from high-order AR processes and outperforms **FIT** in the low transmission power regime, it still struggles due to the neglect of inter-subcarrier and inter-antenna correlations. As a result, **VKF** fails to achieve a TNMSE below -5 dB at $P_T = 24$ dBm, even at $v = 60$ km/h. By exploiting statistical CSI by LMMSE estimators and modeling temporal correlations with the Prony method, **PAD** outperforms both **FIT** and **VKF** across the full transmission power range, with only marginal inferiority to **FIT** at $P_T = 24$ dBm and $v = 60$ km/h. Among the proposed algorithms, **online TS-DCP** in Algorithm 3 is superior to both **Online TS-DCP (PS)** and **Online TS-DCP**

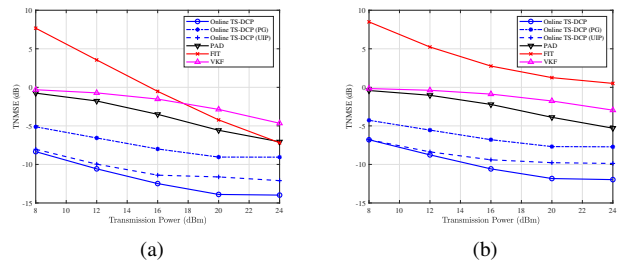


Fig. 6. TNMSE of channel prediction versus transmission power: (a) $v = 60$ km/h, (b) $v = 120$ km/h.

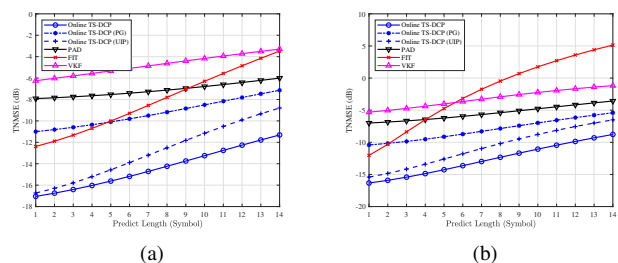


Fig. 7. TNMSE of channel prediction versus predict length for $P_T = 24$ dBm: (a) $v = 60$ km/h, (b) $v = 120$ km/h.

(**UIP**), owing to the generator learning and structured prior. Notably, the proposed algorithms still significantly outperform all benchmarks, even with pre-sampled generators and the unstructured independent prior, highlighting the improvement of channel prediction performance by Doppler domain modeling.

2) *TNMSE for Different Prediction Length*: To illustrate the variation of channel prediction performance with prediction length, we provide the performance for symbols between the current pilot symbols and the first future pilot symbols in Fig. 7. As expected, the performance of the proposed algorithms and the benchmarks deteriorates with increasing prediction length, which is consistent with prior channel prediction studies. Since **FIT** captures the temporal correlations by first-order Taylor series, the modeling error rises with the increasing prediction length, leading to an 8 dB drop in TNMSE at $v = 60$ km/h and a 15 dB drop at $v = 120$ km/h. In contrast, the TNMSE of **PAD** is more stable with increasing prediction length, which suggests that the Prony method provides a more accurate model for temporal correlations in moderate- to high-mobility scenarios. Limited by the under-exploration of inter-antenna and inter-subcarrier correlations, the **VKF** struggles to achieve satisfactory performance at all prediction lengths. Due to the gridless ALS algorithm employed in **FIT**, **Online TS-DCP (PS)** is slightly inferior to **FIT** for short prediction length, demonstrating the necessity of generator learning. Notably, **Online TS-DCP** and **Online TS-**

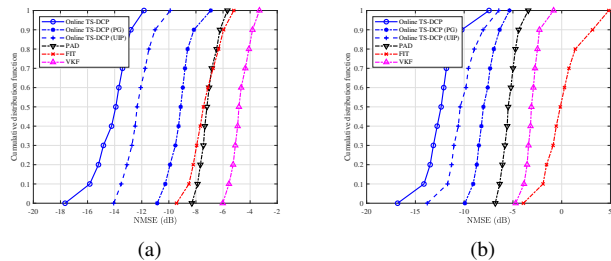


Fig. 8. CDF of channel prediction error for $P_T = 24$ dBm: (a) $v = 60$ km/h, (b) $v = 120$ km/h.

DCP (UIP) outperform all benchmarks across the prediction lengths. Specifically, for the first future non-pilot symbols and pilot symbols, **Online TS-DCP** achieves TNMSEs below -16 dB and -11 dB at $v = 60$ km/h and below -15 dB and -9 dB at $v = 120$ km/h, which are unattainable by all other algorithms. The TNMSE gap between **Online TS-DCP (UIP)** and **Online TS-DCP** widens to more than 2 dB with increasing prediction length, indicating that the structured prior contributes to the acquisition of more accurate angle-delay-Doppler domain channels.

3) *CDF of Prediction Errors*: In Fig. 8, we present the cumulative distribution function (CDF) of the prediction errors, measured in terms of normalized mean square error (NMSE), for the proposed algorithms and benchmarks. **FIT** and **PAD** exhibit similar prediction error distributions at $v = 60$ km/h, while **FIT** is inferior to **PAD** at $v = 120$ km/h, but both outperform **VKF**. This highlights the inaccuracy of the first-order Taylor series in modeling temporal correlations at high mobility and underscores the importance of capturing inter-antenna and inter-subcarrier correlations for accurate channel prediction. Furthermore, **Online TS-DCP (PS)**, **Online TS-DCP (UIP)**, and **Online TS-DCP** achieve the lowest prediction error for both mobility scenarios. Specifically, the 90-th percentile of the prediction error for these algorithms is below -12.5 dB, -11 dB, and -8 dB at $v = 60$ km/h, and below -10 dB, -7 dB, and -6 dB at $v = 120$ km/h, respectively.

4) *Convergence Behaviors*: To observe the trend of channel prediction performance with respect to the number of iterations, we present the convergence performance of **Online TS-DCP**, **Online TS-DCP (UIP)**, and **Online TS-DCP (PG)** at $P_T = 24$ dBm in Fig. 9, separating the initial and tracking phases. It is evident that **Online TS-DCP** and **Online TS-DCP (UIP)** exhibit fast convergence rates and achieve favorable convergence results in both phases, owing to the model accuracy improvement enabled by generator learning. Compared to **Online TS-DCP (PG)**, **Online TS-DCP** and **Online TS-DCP (UIP)** reduce the TNMSE from approximately -9 dB to nearly -12 dB and -13 dB at $v = 60$ km/h, respectively, while from about -8 dB to below -9.5 dB and -11 dB at $v = 120$ km/h, respectively. Besides, the structured prior design in **Online TS-DCP** and **Online TS-DCP (PG)** enables a rapid reduction in TNMSE during the initial iterations of the tracking phase, allowing for early termination to reduce computational complexity based on practical system performance requirements. Specifically, in the early iterations of

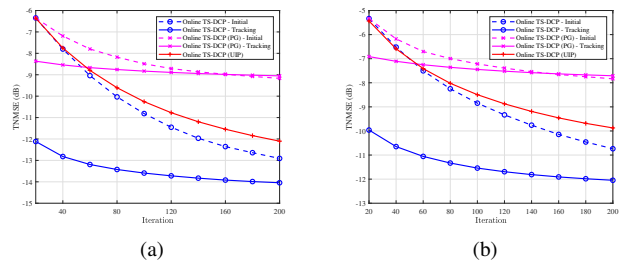


Fig. 9. The convergence performance of the proposed algorithms for $P_T = 24$ dBm: (a) $v = 60$ km/h, (b) $v = 120$ km/h.

the tracking phase, **Online TS-DCP** and **Online TS-DCP (PG)** achieve the TNMSE gains approximately $1.5\sim 2$ dB and $4.5\sim 5.5$ dB compared to the initial phase, respectively, with the gap narrowing as the number of iterations increases.

VII. CONCLUSION

This paper investigated TS-DCP for massive MIMO with temporal non-stationarity in moderate- to high-mobility scenarios. Specifically, by framing the pilot symbols, we captured intra-frame and inter-frame correlations through Doppler domain modeling and Markov/AR processes, respectively. Besides, we upgraded the Markov process and CGD to MRF and TCGD, modeling significant cross-domain correlations of the sparsity and power in the angle-delay-Doppler domain channel. Building on the probabilistic models, the TS-DCP was formulated as the VFE minimization problem, incorporating online approximations and the Bethe method to balance exactness and tractability. By leveraging the multilinear structure of channels, the proposed online TS-DCP algorithm achieved substantial reductions in computational complexity. Numerical results demonstrated significant superiority of proposed algorithms over benchmarks in channel prediction performance. In the future, we will investigate channel prediction algorithms for massive MIMO systems with spatial non-stationarity, focusing on the challenges of inter-antenna correlation modeling.

REFERENCES

- [1] T. L. Marzetta, "Noncooperative cellular wireless with unlimited numbers of base station antennas," *IEEE Trans. Wireless Commun.*, vol. 9, no. 11, pp. 3590–3600, Nov. 2010.
- [2] L. Lu, G. Y. Li *et al.*, "An overview of massive MIMO: Benefits and challenges," *IEEE J. Sel. Topics Signal Process.*, vol. 8, no. 5, pp. 742–758, Oct. 2014.
- [3] E. Björnson, J. Hoydis, and L. Sanguinetti, "Massive MIMO has unlimited capacity," *IEEE Trans. Wireless Commun.*, vol. 17, no. 1, pp. 574–590, Jan. 2018.
- [4] L. Sanguinetti, E. Björnson, and J. Hoydis, "Toward massive MIMO 2.0: Understanding spatial correlation, interference suppression, and pilot contamination," *IEEE Trans. Commun.*, vol. 68, no. 1, pp. 232–257, Jan. 2020.
- [5] H. Jin, K. Liu *et al.*, "Massive MIMO evolution towards 3GPP Release 18," *IEEE J. Sel. Areas Commun.*, vol. 41, no. 6, pp. 1635–1654, Jun. 2023.
- [6] A. Liu, L. Lian *et al.*, "Downlink channel estimation in multiuser massive MIMO with hidden Markovian sparsity," *IEEE Trans. Signal Process.*, vol. 66, no. 18, pp. 4796–4810, Sep. 2018.
- [7] H. Lee, H. Choi *et al.*, "Downlink channel reconstruction for spatial multiplexing in massive MIMO systems," *IEEE Trans. Wireless Commun.*, vol. 20, no. 9, pp. 6154–6166, Sep. 2021.

- [8] Y. Zhu, G. Sun *et al.*, “OFDM-based massive grant-free transmission over frequency-selective fading channels,” *IEEE Trans. Commun.*, vol. 70, no. 7, pp. 4543–4558, Jul. 2022.
- [9] H. Miao, J. Zhang *et al.*, “Sub-6 GHz to mmWave for 5G-advanced and beyond: Channel measurements, characteristics and impact on system performance,” *IEEE J. Sel. Areas Commun.*, vol. 41, no. 6, pp. 1945–1960, Jun. 2024.
- [10] D. Shakya, M. Ying *et al.*, “Propagation measurements and channel models in indoor environment at 6.75 GHz FR1 (C) and 16.95 GHz FR3 upper-mid band spectrum for 5G and 6G,” *arXiv preprint arXiv:2405.01358*, 2024.
- [11] R. O. Adeogun, P. D. Teal, and P. A. Dmochowski, “Extrapolation of MIMO mobile-to-mobile wireless channels using parametric-model-based prediction,” *IEEE Trans. Veh. Technol.*, vol. 64, no. 10, pp. 4487–4498, Oct. 2015.
- [12] R. Adeogun, P. Teal, and P. Dmochowski, “Parametric schemes for prediction of wideband MIMO wireless channels,” *arXiv preprint arXiv:1408.0581*, 2014.
- [13] H. Yin, H. Wang *et al.*, “Addressing the curse of mobility in massive MIMO with prony-based angular-delay domain channel predictions,” *IEEE J. Sel. Areas Commun.*, vol. 38, no. 12, pp. 2903–2917, Dec. 2020.
- [14] Z. Qin, H. Yin *et al.*, “A partial reciprocity-based channel prediction framework for FDD massive MIMO with high mobility,” *IEEE Trans. Wireless Commun.*, vol. 21, no. 11, pp. 9638–9652, Nov. 2022.
- [15] W. Li, H. Yin *et al.*, “A multi-dimensional matrix pencil-based channel prediction method for massive MIMO with mobility,” *IEEE Trans. Wireless Commun.*, vol. 22, no. 4, pp. 2215–2230, Apr. 2023.
- [16] Y. Zhu, J. Zhuang *et al.*, “Joint channel estimation and prediction for massive MIMO with frequency hopping sounding,” *arXiv preprint arXiv:2406.09053*, 2024.
- [17] D. Shi, L. Song *et al.*, “Channel acquisition for HF skywave massive MIMO-OFDM communications,” *IEEE Trans. Wireless Commun.*, vol. 22, no. 6, pp. 4074–4089, Jun. 2023.
- [18] X. Wang, Y. Shi *et al.*, “Channel prediction with time-varying Doppler spectrum in high-mobility scenarios: A polynomial fourier transform based approach and field measurements,” *IEEE Trans. Wireless Commun.*, vol. 22, no. 11, pp. 7116–7129, Nov. 2023.
- [19] Y. Wan, G. Liu *et al.*, “Robust multi-user channel tracking scheme for 5G new radio,” *IEEE Trans. Wireless Commun.*, 2023.
- [20] Y. Wan and A. Liu, “A two-stage 2D channel extrapolation scheme for TDD 5G NR systems,” *IEEE Trans. Wireless Commun.*, 2024.
- [21] J. Ma, S. Zhang *et al.*, “Sparse Bayesian learning for the time-varying massive MIMO channels: Acquisition and tracking,” *IEEE Trans. Commun.*, vol. 67, no. 3, pp. 1925–1938, Mar. 2019.
- [22] M. Li, S. Zhang *et al.*, “Time-varying massive MIMO channel estimation: Capturing, reconstruction, and restoration,” *IEEE Trans. Commun.*, vol. 67, no. 11, pp. 7558–7572, Nov. 2019.
- [23] S. Srivastava, M. S. Kumar *et al.*, “Sparse doubly-selective channel estimation techniques for OSTBC MIMO-OFDM systems: A hierarchical Bayesian Kalman filter based approach,” *IEEE Trans. Commun.*, vol. 68, no. 8, pp. 4844–4858, Aug. 2020.
- [24] S. Srivastava, C. S. K. Patro *et al.*, “Sparse, group-sparse, and online Bayesian learning aided channel estimation for doubly-selective mmWave hybrid MIMO OFDM systems,” *IEEE Trans. Commun.*, vol. 69, no. 9, pp. 5843–5858, Sep. 2021.
- [25] C. Wu, X. Yi *et al.*, “Channel prediction in high-mobility massive MIMO: From spatio-temporal autoregression to deep learning,” *IEEE J. Sel. Areas Commun.*, vol. 39, no. 7, pp. 1915–1930, Jul. 2021.
- [26] H. Kim, S. Kim *et al.*, “Massive MIMO channel prediction: Kalman filtering vs. machine learning,” *IEEE Trans. Commun.*, vol. 69, no. 1, pp. 518–528, Jan. 2021.
- [27] P. Wang, J. Li *et al.*, “Two-stage based partial online optimization channel prediction for massive MIMO in high-mobility,” *IEEE Commun. Lett.*, vol. 28, no. 2, pp. 417–421, Feb. 2024.
- [28] J. Zhao, H. Xie *et al.*, “Time varying channel tracking with spatial and temporal BEM for massive MIMO systems,” *IEEE Trans. Wireless Commun.*, vol. 17, no. 8, pp. 5653–5666, Aug. 2018.
- [29] L. Lian, A. Liu, and V. K. Lau, “Exploiting dynamic sparsity for downlink FDD-massive MIMO channel tracking,” *IEEE Trans. Signal Process.*, vol. 67, no. 8, pp. 2007–2021, Apr. 2019.
- [30] X. Liu, W. Wang *et al.*, “Sparse channel estimation via hierarchical hybrid message passing for massive MIMO-OFDM systems,” *IEEE Trans. Wireless Commun.*, vol. 20, no. 11, pp. 7118–7134, Nov. 2021.
- [31] W. Peng, W. Li *et al.*, “Downlink channel prediction for time-varying FDD massive MIMO systems,” *IEEE J. Sel. Topics Signal Process.*, vol. 13, no. 5, pp. 1090–1102, Sep. 2019.
- [32] X. Cheng, Z. Huang, and L. Bai, “Channel nonstationarity and consistency for beyond 5G and 6G: A survey,” *IEEE Commun. Surveys Tuts.*, vol. 24, no. 3, pp. 1634–1669, 3rd Quart. 2022.
- [33] Z. Huang, X. Cheng, and X. Yin, “A general 3D non-stationary 6G channel model with time-space consistency,” *IEEE Trans. Commun.*, vol. 70, no. 5, pp. 3436–3450, May 2022.
- [34] H. Hou, Y. Wang *et al.*, “Joint beam alignment and Doppler estimation for fast time-varying wideband mmWave channels,” *IEEE Trans. Wireless Commun.*, vol. 23, no. 9, pp. 10895–10910, Sep. 2024.
- [35] J. Bian, C.-X. Wang *et al.*, “A general 3D non-stationary wireless channel model for 5G and beyond,” *IEEE Trans. Wireless Commun.*, vol. 20, no. 5, pp. 3211–3224, May 2021.
- [36] —, “A novel 3D beam domain channel model for massive MIMO communication systems,” *IEEE Trans. Wireless Commun.*, vol. 22, no. 3, pp. 1618–1632, Mar. 2023.
- [37] T. G. Kolda and B. W. Bader, “Tensor decompositions and applications,” *SIAM Review*, vol. 51, no. 3, pp. 455–500, 2009.
- [38] J. B. Kruskal, “Three-way arrays: Rank and uniqueness of trilinear decompositions, with application to arithmetic complexity and statistics,” *Linear Algebra Appl.*, vol. 18, no. 2, pp. 95–138, 1977.
- [39] M. Sørensen and L. De Lathauwer, “Blind signal separation via tensor decomposition with Vandermonde factor: Canonical polyadic decomposition,” *IEEE Trans. Signal Process.*, vol. 61, no. 22, pp. 5507–5519, Nov. 2013.
- [40] J. H. d. M. Goulart, M. Boizard *et al.*, “Tensor CP decomposition with structured factor matrices: Algorithms and performance,” *IEEE J. Sel. Topics Signal Process.*, vol. 10, no. 4, pp. 757–769, Jun. 2015.
- [41] J. E. Cohen and N. Gillis, “Dictionary-based tensor canonical polyadic decomposition,” *IEEE Trans. Signal Process.*, vol. 66, no. 7, pp. 1876–1889, Apr. 2017.
- [42] W.-C. Chang and Y. T. Su, “Sparse Bayesian learning based tensor dictionary learning and signal recovery with application to MIMO channel estimation,” *IEEE J. Sel. Topics Signal Process.*, vol. 15, no. 3, pp. 847–859, Apr. 2021.
- [43] L. Cheng, Z. Chen *et al.*, “Towards flexible sparsity-aware modeling: Automatic tensor rank learning using the generalized hyperbolic prior,” *IEEE Trans. Signal Process.*, vol. 70, pp. 1834–1849, Apr. 2022.
- [44] X. Xu, S. Zhang *et al.*, “Sparse Bayesian learning based channel extrapolation for RIS assisted MIMO-OFDM,” *IEEE Trans. Commun.*, vol. 70, no. 8, pp. 5498–5513, Aug. 2022.
- [45] M. Zhang, X. Yuan, and Z.-Q. He, “Variance state propagation for structured sparse Bayesian learning,” *IEEE Trans. Signal Process.*, vol. 68, pp. 2386–2400, 2020.
- [46] W. Xu, Y. Xiao *et al.*, “Joint scattering environment sensing and channel estimation based on non-stationary Markov random field,” *IEEE Trans. Wireless Commun.*, vol. 23, no. 5, pp. 3903–3917, May 2023.
- [47] X. Liu, W. Wang *et al.*, “Structured hybrid message passing based channel estimation for massive MIMO-OFDM systems,” *IEEE Trans. Veh. Technol.*, vol. 72, no. 6, pp. 7491–7507, Jun. 2023.
- [48] J. Ziniel and P. Schniter, “Dynamic compressive sensing of time-varying signals via approximate message passing,” *IEEE Trans. Signal Process.*, vol. 61, no. 21, pp. 5270–5284, Nov. 2013.
- [49] J. S. Yedidia, W. T. Freeman, and Y. Weiss, “Constructing free-energy approximations and generalized belief propagation algorithms,” *IEEE Trans. Inf. Theory*, vol. 51, no. 7, pp. 2282–2312, Jul. 2005.
- [50] D. Zhang, X. Song *et al.*, “Unifying message passing algorithms under the framework of constrained Bethe free energy minimization,” *IEEE Trans. Wireless Commun.*, vol. 20, no. 7, pp. 4144–4158, Jul. 2021.
- [51] H. Hou, X. He *et al.*, “Beam-delay domain channel estimation for mmWave XL-MIMO systems,” *IEEE J. Sel. Topics Signal Process.*, vol. 18, no. 4, pp. 646–661, May 2024.
- [52] S. P. Boyd and L. Vandenberghe, *Convex Optimization*. Cambridge University Press, 2004.
- [53] J. Fang, Y. Shen *et al.*, “Pattern-coupled sparse Bayesian learning for recovery of block-sparse signals,” *IEEE Trans. Signal Process.*, vol. 63, no. 2, pp. 360–372, Jan. 2015.
- [54] J. Fang, L. Zhang, and H. Li, “Two-dimensional pattern-coupled sparse Bayesian learning via generalized approximate message passing,” *IEEE Trans. Image Process.*, vol. 25, no. 6, pp. 2920–2930, Jun. 2016.
- [55] 3GPP, “Study on channel model for frequencies from 0.5 to 100 GHz (release 16),” *Technical Report TR 38.901*, 2020.
- [56] S. Jaeckel, L. Raschkowski *et al.*, “QuaDRiGa: A 3-D multi-cell channel model with time evolution for enabling virtual field trials,” *IEEE Trans. Antennas Propag.*, vol. 62, no. 6, pp. 3242–3256, Jun. 2014.
- [57] X. Dong, W.-S. Lu, and A. C. Soong, “Linear interpolation in pilot symbol assisted channel estimation for OFDM,” *IEEE Trans. Wireless Commun.*, vol. 6, no. 5, pp. 1910–1920, May 2007.